ARTICLES
https://doi.org/10.1038/s41556-017-0022-y

nature cell biology

RIP3 targets pyruvate dehydrogenase complex to increase aerobic respiration in TNF-induced necroptosis

Zhentao Yang[1], Yan Wang[1], Yingying Zhang[1], Xiadi He[2], Chuan-Qi Zhong[1], Hengxiao Ni[1], Xin Chen[1], Yaoji Liang[1], Jianfeng Wu[1], Shimin Zhao[2], Dawang Zhou[1] and Jiahuai Han[1]*

Receptor-interacting protein kinase 3 (RIP3)-regulated production of reactive oxygen species (ROS) positively feeds back on tumour necrosis factor (TNF)-induced necroptosis, a type of programmed necrosis. Glutamine catabolism is known to contribute to RIP3-mediated ROS induction, but the major contributor is unknown. Here, we show that RIP3 activates the pyruvate dehydrogenase complex (PDC, also known as PDH), the rate-limiting enzyme linking glycolysis to aerobic respiration, by directly phosphorylating the PDC E3 subunit (PDC-E3) on T135. Upon activation, PDC enhances aerobic respiration and subsequent mitochondrial ROS production. Unexpectedly, mixed-lineage kinase domain-like (MLKL) is also required for the induction of aerobic respiration, and we further show that it is required for RIP3 translocation to meet mitochondria-localized PDC. Our data uncover a regulation mechanism of PDC activity, show that PDC activation by RIP3 is most likely the major mechanism activated by TNF to increase aerobic respiration and its by-product ROS, and suggest that RIP3-dependent induction of aerobic respiration contributes to pathologies related to oxidative stress.

Tumour necrosis factor-α (TNF-α) can induce either apoptosis or necroptosis in different cell lines[1]. Apoptosis is characterized by cell shrinkage, nuclei breakdown and formation of apoptotic bodies[2], while necroptosis involves cell membrane rupture and requires the formation of a multiple protein complex called the necrosome[3–5]. The interaction between receptor-interacting protein kinase 1 (RIP1) and RIP3, two core components of the necrosome[3–5], leads to RIP3–RIP3 homo-interaction and RIP3 autophosphorylation[6–8]. The phosphorylated RIP3 recruits and phosphorylates mixed lineage kinase domain-like (MLKL)[9,10], which then translocates to the cell membrane to execute necroptosis[11–14].

Reactive oxygen species (ROS) have long been considered a driving force for necroptosis[15–17], but recent studies concluded that ROS are not involved in the necroptosis of all cell types, because ROS are dispensable for necroptosis in some cell lines[4,18,19]. The major function of ROS in necroptosis is to enhance necrosome formation[19,20]. Oxidation of specific cysteines in RIP1 by ROS activates RIP1 autophosphorylation, promoting the formation of functional necrosome[20]. Mitochondrial ROS are known to participate in necroptosis[15], and the involvement of NADPH oxidase (Nox1) in necroptosis has also been reported[21]. Our previous study showed that TNF-induced ROS production is RIP3-dependent, and the metabolic enzymes glycogen phosphorylase (PYGL), glutamate-ammonia ligase (GLUL) and glutamate dehydrogenase 1 (GLUD1) are targets of RIP3, contributing to TNF-induced ROS[3]. However, how RIP3 regulates ROS production is still largely unknown.

The production of mitochondrial ROS is associated with aerobic respiration[22–24]. Decarboxylation of pyruvate to acetyl coenzyme A (acetyl-CoA) in mitochondria by the pyruvate dehydrogenase complex PDC (also known as PDH) links glycolysis to the Krebs cycle and controls the rate of aerobic respiration[25]. PDC regulation involves cyclic phosphorylation and dephosphorylation of the PDC-E1 subunit by pyruvate dehydrogenase kinases (PDKs) and pyruvate dehydrogenase phosphatases (PDPs), respectively[26]. The changes in PDC activity play an important role in many biological processes such as cancer metabolism and senescence[27,28].

Here, we report that PDC can be activated by RIP3, which is an additional, and most likely major, mechanism of TNF-induced upregulation of aerobic respiration. RIP3-MLKL-containing necrosome can translocate to the mitochondria, and phosphorylation of the PDC-E3 subunit in mitochondria is a regulation mechanism of PDC activation. The activation of PDC increases aerobic respiration, which generates ROS. ROS in turn enhance necrosome formation and thereafter necroptosis.

Results

TNF induces RIP3-dependent increase in aerobic respiration. TNF-induced ROS production is RIP3-dependent[3]. Because most mitochondrial ROS are the by-products of aerobic respiration[22–24], we measured this, using the Seahorse XF^e 96 analyser (see Methods) to measure the oxygen consumption rate (OCR) in TNF-stimulated cells. A pan-caspase inhibitor z-Val-Ala-DL-Asp-fluoromethylketone (zVAD or Z) was included to eliminate apoptosis. Smac mimetic (S) was included for some cell lines, as TNF-induced necroptosis of these cell types cannot occur without it. The following cell line pairs—murine fibroblast L929 and its *RIP3* knockout (KO) line, murine macrophage RAW264.7 cell line and its *RIP3* KO line, murine embryonic fibroblast (MEF) and *RIP3* KO MEF, RIP3-expressing NIH3T3-A (A+RIP3) and NIH3T3-A (A+vector) cell line, RIP3-expressing HeLa (HeLa+RIP3) and HeLa (HeLa+vector) cell line, HT-29 and its *RIP3* KO cell line—were used. As shown in Fig. 1a–e, OCR was increased in L929, RAW264.7, MEF,

---

[1]State Key Laboratory of Cellular Stress Biology, Innovation Center for Cell Signaling Network, School of Life Sciences, Xiamen University, Xiamen, Fujian, China. [2]State Key Laboratory of Genetic Engineering, School of Life Science and Institute of Biomedical Sciences, The Obstetrics & Gynecology Hospital of Fudan University, Shanghai, China. *e-mail: jhan@xmu.edu.cn

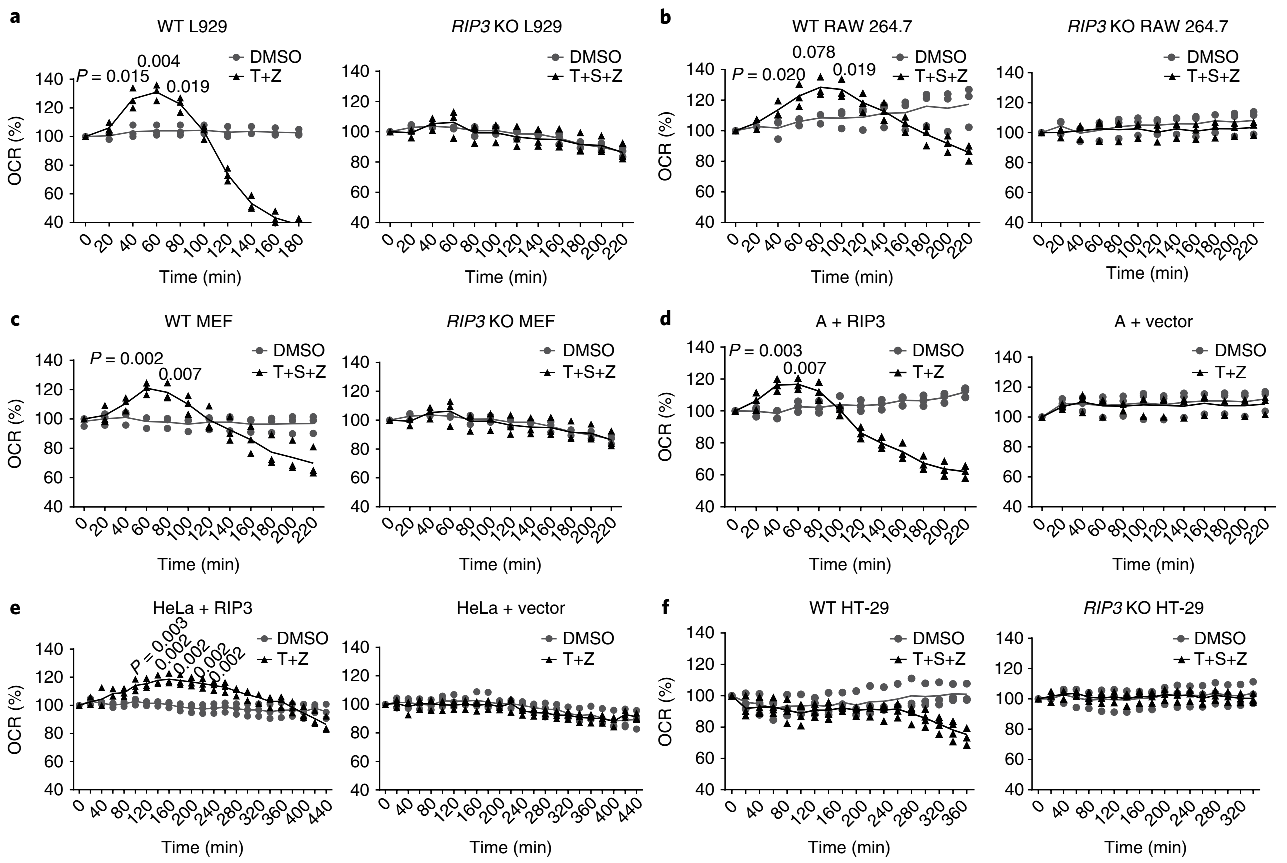

Fig. 1 | TNF induces an increase in aerobic respiration in a RIP3-dependent manner. a, Relative oxygen consumption rates (OCRs) of WT and *RIP3* KO L929 cells treated with DMSO or TNF (T, 10 $\mathrm{ng\,ml^{-1}}$) + zVAD (Z, 20 μM), measured over time using a Seahorse XF^e 96 analyser. The basal level of oxygen consumption was set as 100%. **b**,**c**, OCRs of WT and *RIP3* KO RAW264.7 cells (**b**) or WT and *RIP3* KO MEF (**c**) treated with DMSO or TNF (10 $\mathrm{ng\,ml^{-1}}$) + Smac mimetic (S, 1 μM) + zVAD (20 μM), measured over time. **d**,**e**, NIH 3T3-A cells (**d**) or HeLa cells (**e**) were infected with a lentivirus encoding nothing (vector) or RIP3 for 96 h and then treated with DMSO or TNF (30 $\mathrm{ng\,ml^{-1}}$) + zVAD (20 μM). OCR was measured over time. **f**, OCRs of WT and *RIP3* KO HT-29 cells treated with DMSO or TNF (30 $\mathrm{ng\,ml^{-1}}$) + Smac mimetic (1 μM) + zVAD (20 μM), measured over time. Data are from $n = 3$ independent experiments. Two-tailed Student's *t*-test was applied for the indicated *P* values. Statistics source data are provided in Supplementary Table 1.

A+RIP3 and HeLa+RIP3 cell lines at certain time points after TNF treatment, and dropped later. In contrast, OCR was not changed in counterpart cell lines with no RIP3 expression. TNF did not increase OCR in HT-29 (Fig. 1f), and there was no effect of RIP3 deletion (Fig. 1f). The drop in the OCR in RIP3-expressing cells at late time points after TNF treatment is most probably due to the loss of living cells (Fig. 2a).

As zVAD was reported to have effects beyond caspase 8 inhibition[29], we generated a *caspase 8* KO L929 cell line. As expected, the level of TNF-induced death in wild-type (WT) L929 cells is much less than that induced by TNF+zVAD. The level of TNF-induced cell death of *caspase 8* KO cells was similar to that of TNF+zVAD-treated WT L929 cells, and zVAD addition did not enhance TNF-induced death in *caspase 8* KO cells (Fig. 2b). We then detected an increase of OCR in TNF-treated WT L929 cells, and addition of zVAD enhanced the increase (Fig. 2c). TNF treatment of *caspase 8* KO cells induced OCR to a level similar to that induced by TNF+zVAD in WT L929 cells, and zVAD did not enchance OCR in TNF-treated *caspase 8* KO cells (Fig. 2c). In addition, the use of qVD, another caspase-inhibitor, yielded the same result as using zVAD (Fig. 2c). Thus, the enhancing effect of zVAD on TNF-induced OCR increase is due to the inhibition of caspase 8.

We measured mitochondrial ROS using a fluorogenic dye MitoSOX Red, which stains mitochondrial superoxide in living cells, and obtained results similar to those in published studies (Supplementary Fig. 1a)[3,4,15]. Importantly, TNF only increased the OCR in cell lines in which ROS production can be induced by TNF (Fig. 1 and Supplementary Fig. 1a), and both OCR and ROS induction were RIP3-dependent. This result is supported by data obtained by using mitochondria-localized redox-sensitive green fluorescent protein (mito-roGFP)[30] to measure ROS in living cells (Supplementary Fig. 1b). Thus, TNF induces an increase in RIP3-dependent aerobic respiration and ROS induction during necroptosis.

TNF-induced increase in aerobic respiration is responsible for ROS induction in necroptosis. OCR in TNF-treated L929 cells increased at 40 min after treatment and reached its maximum at 60 min, then dropped below the basal level at ~100 min (Fig. 1a). When normalized to living cells, OCR reached its maximum at 60 min and maintained this level at later time points of TNF treatment (Fig. 3a). ROS induction in living cells shared a similar pattern (Fig. 3b), and cell death proceeded with the increase in ROS and OCR at late time points (Fig. 3a–c). These data indicate a link between the induction of OCR and ROS in TNF-induced necroptosis.

Inhibition of the respiration chain by amytal (complex I inhibitor) or TTFA (thenoyltrifluoroacetone; complex II inhibitor) inhibited ROS production and necroptosis in TNF-treated L929 cells[16] (Fig. 3d). We confirmed mitochondrial ROS involvement in necroptosis by depleting mitochondria with Parkin overexpression in the presence of carbonyl cyanide *m*-chlorophenyl

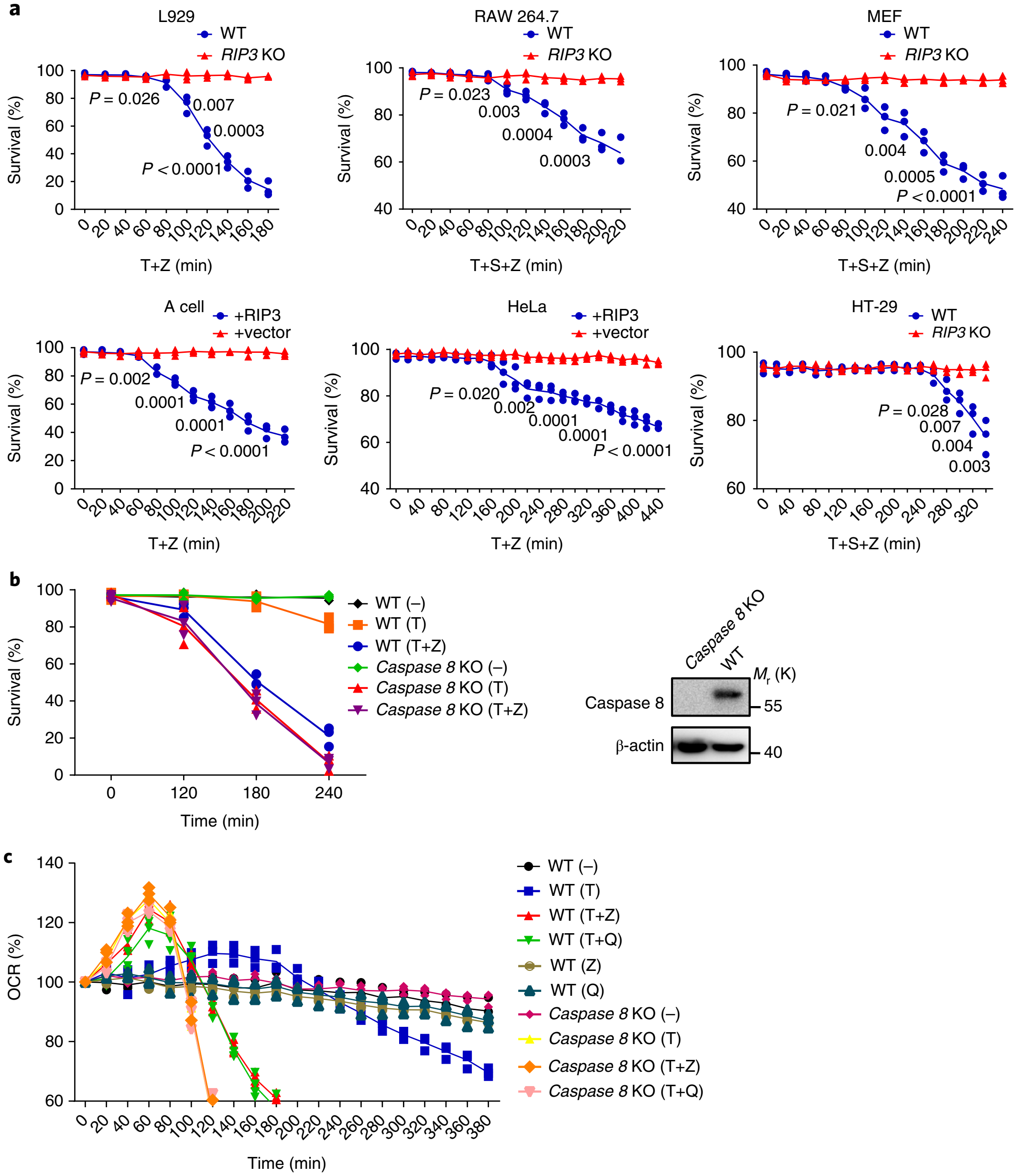

Fig. 2 | Induction of OCR is not due to the side effect of zVAD. a, WT and *RIP3* KO L929 cells (top left), WT and *RIP3* KO RAW 264.7 cells (top middle), WT and *RIP3* KO MEF cells (top right), A + RIP3 or A + vector (bottom left), HeLa + RIP3 or HeLa + vector (bottom middle) and WT and *RIP3* KO HT-29 cells (bottom right) were treated with the indicated stimuli (T, TNF; Z, zVAD; S, Smac) for the indicated periods of time, followed by cell viability analysis. **b**, Left, WT and *caspase 8* KO L929 cells were treated with the indicated stimulus for the indicated periods of time, followed by cell viability analysis. Right, Knockout of *caspase 8* in L929 cells was verified by immunoblotting. **c**, WT and *caspase 8* KO L929 cells were treated with the indicated stimulus followed by OCR measurements over time. Q, qVD (60 μM). Quantitative data are from $n = 3$ independent experiments. In **b**, right, data are representative of three independent experiments. Two-tailed Student's *t*-test was applied for the *P* values. Statistics source data for this figure are provided in Supplementary Table 1.

hydrazone (CCCP, a mitochondrial oxidative phosphorylation uncoupler)[31] (Fig. 3e), which is consistent with the results obtained by mitochondrial DNA depletion by ethidium bromide or chloramphenicol treatment[17]. As reported, ROS scavengers like butylated hydroxyanisole (BHA) or mitoQ inhibited TNF-induced necroptosis (Fig. 3f and Supplementary Fig. 2a). It should be noted that necroptosis could occur without ROS induction in some cell lines[18] (Supplementary Fig. 1a).

Because the level of BHA-mediated inhibition of cell death can be used to measure the contribution of ROS in necroptosis, we analysed the correlation between BHA-mediated inhibition of cell death and OCR increase in all necroptosis-sensitive cells/cell lines available in our laboratory. A very good positive correlation ($R^2 = 0.8968$) between TNF-induced oxygen consumption and the sensitivity to BHA inhibition of necroptosis in those cells was observed (Fig. 3g). As reported[4], BHA could not block TNF-induced necroptosis in HT-29 cells where ROS is not induced nor involved in necroptosis (Fig. 3g). BHA may also inhibit complex I in the respiration chain and lipoxygenases[32], but these possible off-target effects do not contradict the notion that TNF-induced aerobic respiration promotes TNF-induced ROS production and necroptosis.

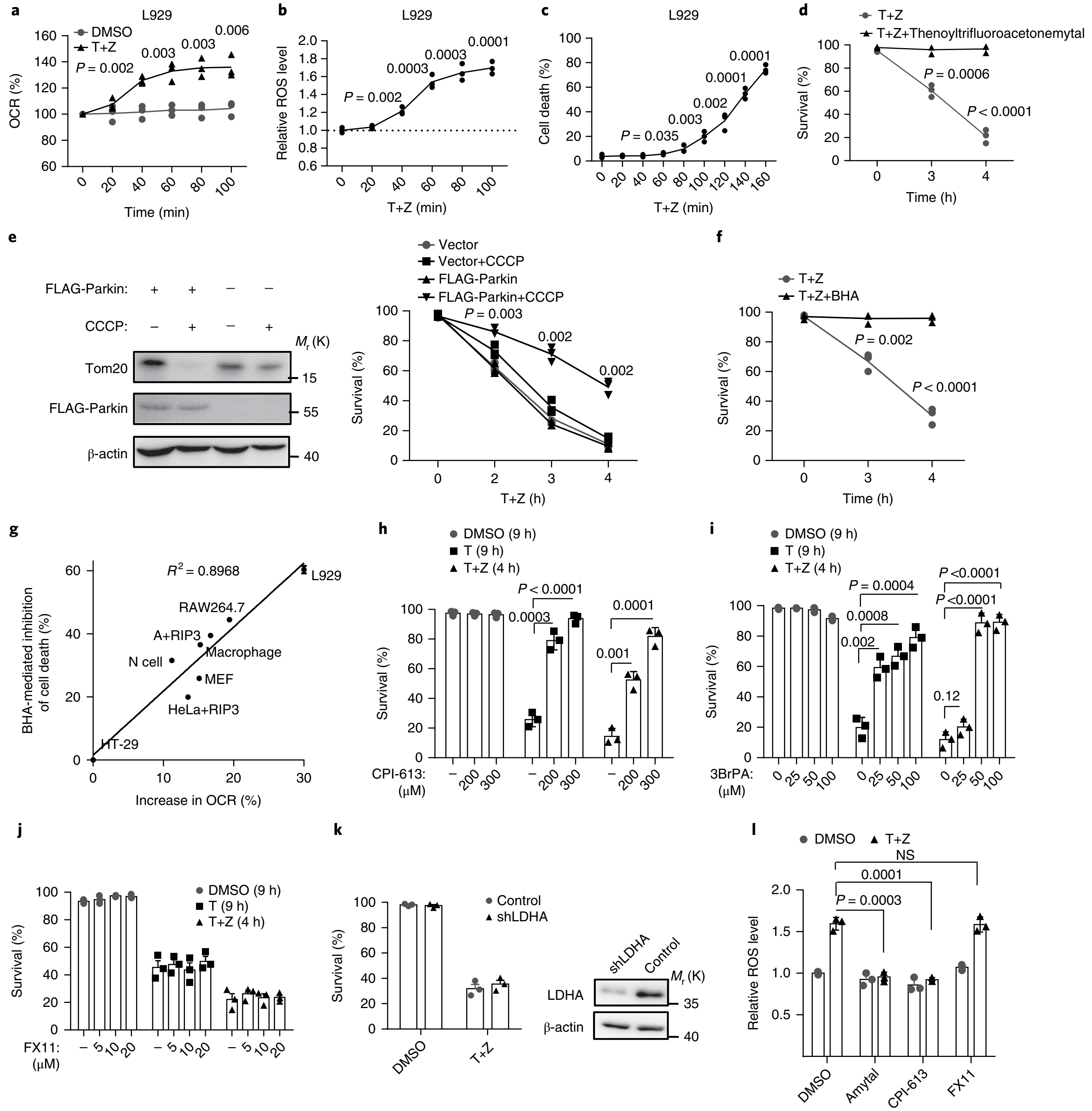

Fig. 3 | TNF-induced increase in aerobic respiration is responsible for ROS induction in necroptosis. a, OCR of L929 cells treated with DMSO or TNF + zVAD, measured over time. At each time point, parallel samples were analysed for cell viability and OCR was normalized to living cells. **b**,**c**, ROS level (**b**) and cell vability (**c**) of L929 cells treated with TNF + zVAD for the indicated periods of time. **d**, L929 cells were pretreated with or without amytal (1 mM) for 1 h and then treated with TNF + zVAD for the indicated periods of time, followed by cell viability analysis. **e**, L929 cells with or without mitochondria depletion were treated with TNF + zVAD, followed by cell viability analysis. Protein levels of Tom20 (mitochondria marker), FLAG-Parkin and β-actin were measured by immunoblotting. **f**, L929 cells were pretreated with or without BHA (100 μM) for 1 h and then treated with TNF + zVAD for the indicated time periods, followed by cell viability analysis. **g**, Correlation curve for BHA-mediated inhibition of cell death and maximum increase in OCR in different cell lines (see Methods for details). $R^2 = 0.8968$ by linear regression analysis of GraphPad Prism. **h**–**j**, L929 cells were pretreated with various doses of a pyruvate dehydrogenase inhibitor CPI-613 (**h**), 3BrPA (**i**) or FX11 (lactate dehydrogenase inhibitor) (**j**) for 4 h, then treated with the indicated stimulus followed by cell viability analysis. **k**, L929 cells with or without knockdown of LDHA (shLDHA) were treated with TNF + zVAD for 4 h followed by cell viability analysis. LDHA protein levels were analysed by immunoblotting. **l**, L929 cells were pretreated with amytal (1 mM), CPI-613 (300 μM) or FX11 (20 μM) for 4 h, then treated with TNF + zVAD for 2 h followed by ROS measurement. TNF, 10 ng ml^{-1}; zVAD, 20 μM. Quantitative data shown are from $n = 3$ independent experiments. Error bars represent mean ± s.e.m. of $n = 3$ independent experiments. Two-tailed Student's *t*-test was applied for the indicated *P* values. For **e** (left) and **k** (right), data shown are representative of three independent experiments. Statistics source data for this figure are provided in Supplementary Table 1. Uncropped images of blots are shown in Supplementary Fig. 8.

Previous studies have shown that RIP3 regulates ROS production by activating PYGL, GLUL and GLUD1[3,33]. PYGL increases the use of glycogen for energy, while GLUL and GLUD1 play a role in using Glu or Gln as energy substrates for respiration. We used [U-^{13}C] glutamine to trace glutamine, and found that production of tricarboxylic acid (TCA) cycle metabolites derived from labelled glutamine (such as [$^{13}C_5$]α-KG and [$^{13}C_4$]malate) were increased in TNF+zVAD-treated WT L929 cells but not in *RIP3* KO L929 cells (Supplementary Fig. 2b), supporting that RIP3 activates glutamine catabolism during necroptosis[3]. In addition, when L929 cells are adapted to medium without Gln, TNF-induced necroptosis was attenuated. However, the adapted cells still displayed OCR and ROS increase and underwent necroptosis after TNF treatment (Supplementary Fig. 2c–e), suggesting that other pathway(s) play(s) major roles in TNF-induced aerobic respiration.

PDC is the key enzyme complex to convert pyruvate to acetyl-CoA and links glycolysis to aerobic respiration, and lactate dehydrogenase (LDH) catalyses pyruvate to lactate for anaerobic fermentation. PDC inhibitor (compound CPI-613)[34] pretreatment strongly blocked TNF- or TNF+zVAD-induced necroptosis in L929 cells (Fig. 3h) and A+RIP3 cells (Supplementary Fig. 2f). The same results were obtained when we used another inhibitor, 3-bromopyruvate (3-BrPA), which works as a pyruvate analogue to inhibit mitochondrial metabolism[35] (Fig. 3i). In contrast, inhibition of fermentation by LDH inhibitor FX11[36] (Fig. 3j) or knockdown of lactate dehydrogenase A (LDHA), did not attenuate necroptosis in L929 cells (Fig. 3k and Supplementary Fig. 2g). Inhibition of PDC by CPI-613 had no effect on TNF or TNF+Smac mimetic-induced apoptosis in A cells or MEF, respectively (Supplementary Fig. 2h). TNF-stimulated ROS induction was eliminated when aerobic respiration was inhibited at different sites like PDC or complex I, but was not affected by inhibition of anaerobic fermentation (Fig. 3l). We then concluded that inhibition of aerobic respiration can effectively inhibit ROS induction in necroptosis.

PDC is positively involved in TNF-induced necroptosis. The PDC complex consists of three functional enzymes: E1(α, β), E2 and E3, and dysfunction of any of these leads to PDC function loss[37]. Knockdown or knockout of PDC-E1α by short-hairpin RNAs (shRNAs) or TALEN gene editing technology in the L929 cell line attenuated TNF- or TNF+zVAD- induced necroptosis (Fig. 4a,b and Supplementary Fig. 3a). Reconstitution of PDC-E1α expression in *PDC-E1α* KO L929 cells restored their sensitivity to necroptosis (Fig. 4c). Similarly, knockout of *PDC-E1β* (Fig. 4d and Supplementary Fig. 3b) or *PDC-E3* (Fig. 4e and Supplementary Fig. 3c) in L929 cells reduced TNF+zVAD- or TNF-induced necroptosis. In addition, pyruvate depletion in cell culture medium attenuated TNF-induced ROS production and necroptosis (Supplementary Fig. 3d,e), and inhibition of transport of pyruvate into mitochondria by UK5099[38], an inhibitor of mitochondrial pyruvate carrier proteins, also inhibited necroptosis (Supplementary Fig. 3f). This observation is not limited to TNF-induced necroptosis, as similar results were obtained in poly-IC+zVAD-induced necroptosis in L929 cells and IFN-γ+zVAD-induced necroptosis in *FADD* KO L929 cells[39] (Supplementary Fig. 3g,h).

RIP3 targets PDC to upregulate aerobic respiration. PDC-E1β was found in RIP3 immunocomplex from TNF-treated cells in our previous study[40]. To test whether RIP3 regulates PDC activity, we determined PDC activity in cells after TNF treatment and found RIP3-dependent PDC activation (Fig. 5a and Supplementary Fig. 4a). Consistently, [U-^{13}C] glucose labelling experiments showed accumulation of glucose-derived 2-carbon-labelled metabolic isotopomers of the TCA cycle ([$^{13}C_2$]citrate, [$^{13}C_2$]α-KG and [$^{13}C_2$] malate) in TNF+zVAD-treated WT L929 cells but not in *RIP3* KO L929 cells (Supplementary Fig. 4b). Based on published studies[27,41], the ratio of labelled [$^{13}C_2$]citrate (emulating PDC product) to [$^{13}C_3$] pyruvate (PDC substrate) in [U-^{13}C] glucose labelling experiment can be used to indicate intracellular PDC activity. The [$^{13}C_2$]citrate/[$^{13}C_3$]pyruvate ratio was increased in TNF+zVAD-treated WT L929 cells but not in *RIP3* KO L929 cells (Fig. 5b). PDC activity, OCR, ROS in living cells and the rate of cell death at various time points after TNF+zVAD treatment are shown in Supplementary Fig. 4c. The induction of PDC activity and OCR was slightly earlier than ROS induction, and all preceded cell death.

Dephosphorylation of phosphorylated S232, S293 or S300 sites of PDC-E1α is known to increase PDC activity[26], but TNF-induced PDC activation should use different mechanism because the phosphorylation levels of S232, S293 and S300 were not changed during TNF+zVAD stimulation (Fig. 5c). Re-expression of WT RIP3 but not kinase-dead RIP3 (RIP3-D143N) in *RIP3* KO L929 cells restored TNF+zVAD-induced PDC activation (Fig. 5d and Supplementary Fig. 4d). RIP3-dependent activation of PDC was also found in HeLa+RIP3 and A+RIP3 cell lines after treatment of TNF+zVAD or TNF+Smac mimetic+zVAD or TNF (Fig. 5e,f and Supplementary Fig. 4e).

We purchased PDC complex purified from porcine heart (SIGMA, P7032) and incubated it with affinity-purified FLAG-RIP3 or FLAG-RIP3 D143N in vitro. Incubation of PDC with FLAG-RIP3 but not FLAG-RIP3 D143N increased PDC enzymatic activity, and RIP3 kinase inhibitor GSK872 inhibited PDC activation by FLAG-RIP3 (Fig. 5g). TNF+zVAD treatment induced RIP3 interaction with PDC, as is evident by the detection of PDC-E1α, E1β, E2 and E3 in the RIP3 immunoprecipitates (Fig. 5h). As anticipated, phospho-MLKL and MLKL were also detected (Fig. 5h). To determine which PDC subunit can directly interact with RIP3, we co-expressed HA-RIP3 with FLAG-PDC-E1α, E1β, E2 or E3 in HEK293T cells and detected the interaction of RIP3 with PDC-E1α (Fig. 5i), E1β (Fig. 5j) and E3 (Fig. 5k), but not E2 (Fig. 5l).

RIP3 activates PDC by phosphorylating PDC-E3 on T135. Recombinant GST-PDC-E1α, E1β, E2 and E3 from *Escherichia coli* were used in in vitro kinase reactions with FLAG-RIP3 or FLAG-RIP3 D143N (kinase dead) as kinase. RIP3 phosphorylated PDC-E3 (Fig. 6a), but not PDC-E1α, E1β or E2 (Supplementary Fig. 5a). Mass spectrometry (MS) identified five potential phosphorylation sites (S114, S128, T129, T135 and T163) (Fig. 6b). These five sites are in the F2 fragment (AA86-171) mapped by in vitro kinase assay using deletion mutants of PDC-E3 (Fig. 6c). Mutation of any of the five sites to alanine could not totally eliminate phosphorylation by RIP3, and only when all five sites were mutated could the phosphorylation be abolished (Fig. 6d).

To determine the functional phosphorylation site of PDC-E3 in cells, we introduced vector, PDC-E3 WT and different PDC-E3 mutants into *PDC-E3* KO L929 cells, and then measured PDC activity, ROS production and cell death before and after TNF+zVAD treatment. PDC-E3 T135A mutation inhibited the TNF+zVAD-induced increase in PDC enzymatic activity (Fig. 6e, top), ROS production and cell death (Fig. 6e, middle and bottom). The fact that PDC-E3 T135A reconstitution still had a positive effect on TNF-induced necroptosis could be due to the fact that the basal activity of PDC-E3 T135A is almost equal to that of PDC-E3 WT (Fig. 6e). Consistently, when phosphorylation mimic mutant T135D was expressed in *PDC-E3* KO L929 cells, we detected high basal PDC activity and ROS compared with WT PDC-E3-reconstituted cells (Fig. 6e). PDC-E3 T135D cells were more sensitive than cells expressing WT PDC-E3 in TNF-induced necroptosis (Fig. 6e). As anticipated, CPI-613 blocked TNF+zVAD-induced death in PDC-E3 T135D and PDC-E3 T135A expressing cells (Supplementary Fig. 5b). The effect of T135A or T135D mutation on poly-IC+zVAD-induced necroptosis obtained the same results (Supplementary Fig. 5c). We also analysed TNF-induced OCR and confirmed that

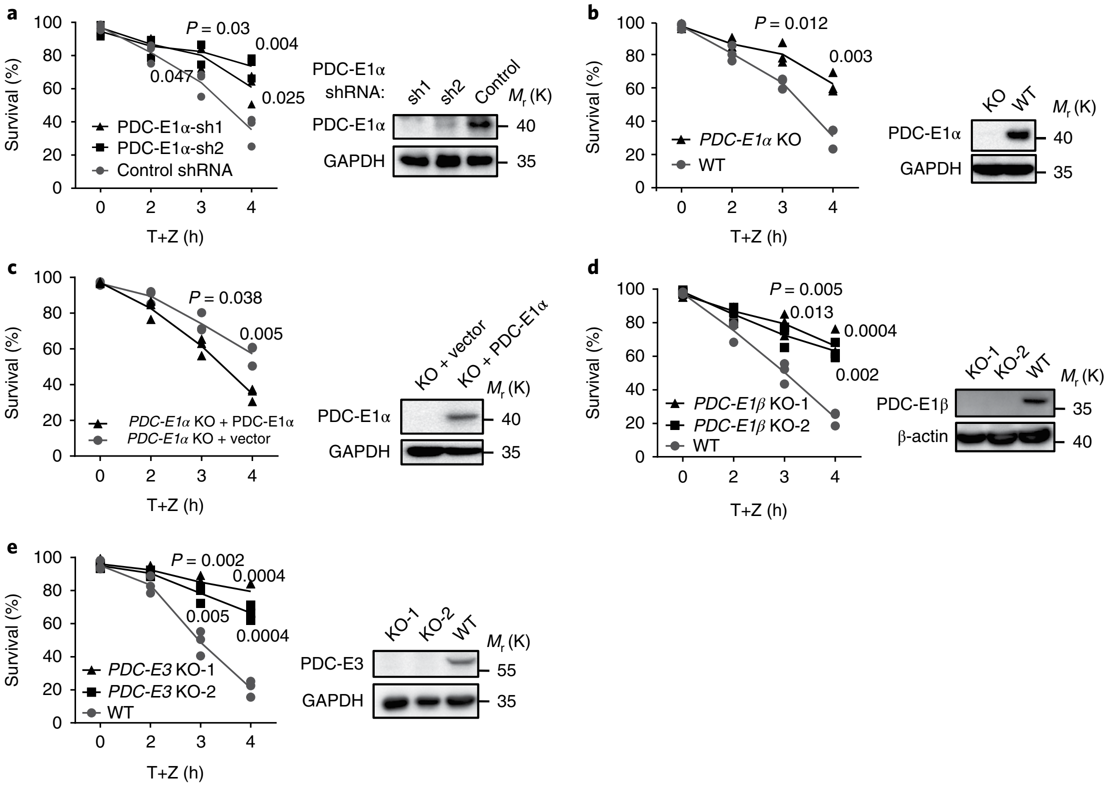

Fig. 4 | PDC is positively involved in TNF-induced necroptosis. a, L929 cells were infected with a lentivirus encoding control or PDC-E1α-shRNA. At 96 h after infection the cells were treated with or without TNF + zVAD for the indicated periods of time, followed by cell viability analysis. PDC-E1α protein levels were analysed by immunoblotting 96 h after infection. **b**, WT and *PDC-E1α* KO L929 cells were treated with or without TNF + zVAD for the indicated periods of time, followed by cell viability analysis. Cell lysates of WT and *PDC-E1α* KO L929 were analysed for protein levels of PDC-E1α by immunoblotting. **c**, *PDC-E1α* KO L929 cells were infected with a lentivirus encoding vector or PDC-E1α. At 96 h after infection, cells were treated with or without TNF + zVAD for indicated periods of time followed by cell viability analysis. Cell lysates were analysed for protein levels of PDC-E1α. **d**,**e**, WT and *PDC-E1β* KO L929 cells (**d**) or WT and *PDC-E3* KO L929 cells (**e**) were treated with or without TNF + zVAD for the indicated periods of time, followed by cell viability analysis. Cell lysates were analysed by immunoblotting for the protein levels of PDC-E1β (**d**) or PDC-E3 (**e**). TNF, 10 ng ml^{-1}; zVAD, 20 μM. Quantitative data are from $n = 3$ independent experiments. Two-tailed Student's t-test was applied for P values. For **a**–**e** (right), data shown are representative of three independent experiments. Statistics source data for this figure are provided in Supplementary Table 1. Uncropped images of blots are shown in Supplementary Fig. 8.

TNF+zVAD could not increase OCR in *PDC-E3* KO+vector cells at all time points, and re-expression of PDC-E3 WT but not T135A mutant restored OCR induction by TNF+zVAD treatment (Fig. 6f). As mentioned earlier in Fig. 1a, the drop of OCR at late time points is due to reduction of living cells. Based on the above data, we concluded that RIP3 phosphorylates PDC-E3 on T135 in TNF-treated L929 cells, which leads to enhanced PDC activity and then an increase in aerobic respiration.

MLKL is required for PDC activation. We measured OCR level after TNF+zVAD treatment in the *MLKL* KO L929 cell line and found that the OCR increase was totally eliminated by *MLKL* deletion (Fig. 7a). Also, knockout of *MLKL* blocked TNF+zVAD-induced PDC activation, ROS production and cell death (Fig. 7b). In *MLKL* KO L929 cell line expressing 3× FLAG-RIP3, TNF+zVAD treatment could not induce interaction between RIP3 and PDC subunits (Fig. 7c). These data suggest that MLKL is required for RIP3 to interact with and activate PDC.

We used stochastic optical reconstruction super-resolution microscopy (STORM) to study RIP3 localization in necroptotic cells. RIP3 was distributed in cytosol in the resting state, and part of RIP3 translocated to mitochondria after stimulation in *MLKL* WT but not *MLKL* KO cells, as is evident by the increase in co-localization between RIP3 and mitochondria (Fig. 7d), consistent with published studies on necrosome localization[11,29]. The interaction between necrosome and mitochondria should be dynamic and transient, which may be the reason for only part of the necrosome being associated with mitochondria. We purified mitochondria from WT and *MLKL* KO cells with or without TNF+zVAD stimulation and found that TNF+zVAD treatment induced translocation of RIP1, RIP3 and MLKL to mitochondria and *MLKL* KO blocked this process (Fig. 7e). To evaluate whether MLKL phosphorylation is required for mitochondria translocation of the necrosome, we reconstituted *MLKL* KO cells with WT and phosphorylation sites mutated MLKL (S345A/S347A)[42], and found that TNF+zVAD-induced translocation of RIP1, RIP3 and MLKL was impaired in MLKL-S345A/S347A-expressing cells (Fig. 7f). Because expression of the gain-of-function mutant of MLKL (MLKL-S345D/347D) caused massive cell death, we used a doxycycline (DOX)-controlled promoter to express it and its WT control in *MLKL* KO L929 cells. As shown in Fig. 7g, DOX-induced expression of MLKL-S345D/347D, unlike MLKL-WT, the induced MLKL-S345D/347D was already localized to mitochondria without TNF stimulation. MLKL-S345D/347D did not bring RIP3 to mitochondria. The expression of MLKL-S345D/347D caused cell death but could not enhance oxygen consumption (Fig. 7h), consistent with a published study that MLKL-S345D/347D-caused necroptosis does not require RIP3[42].

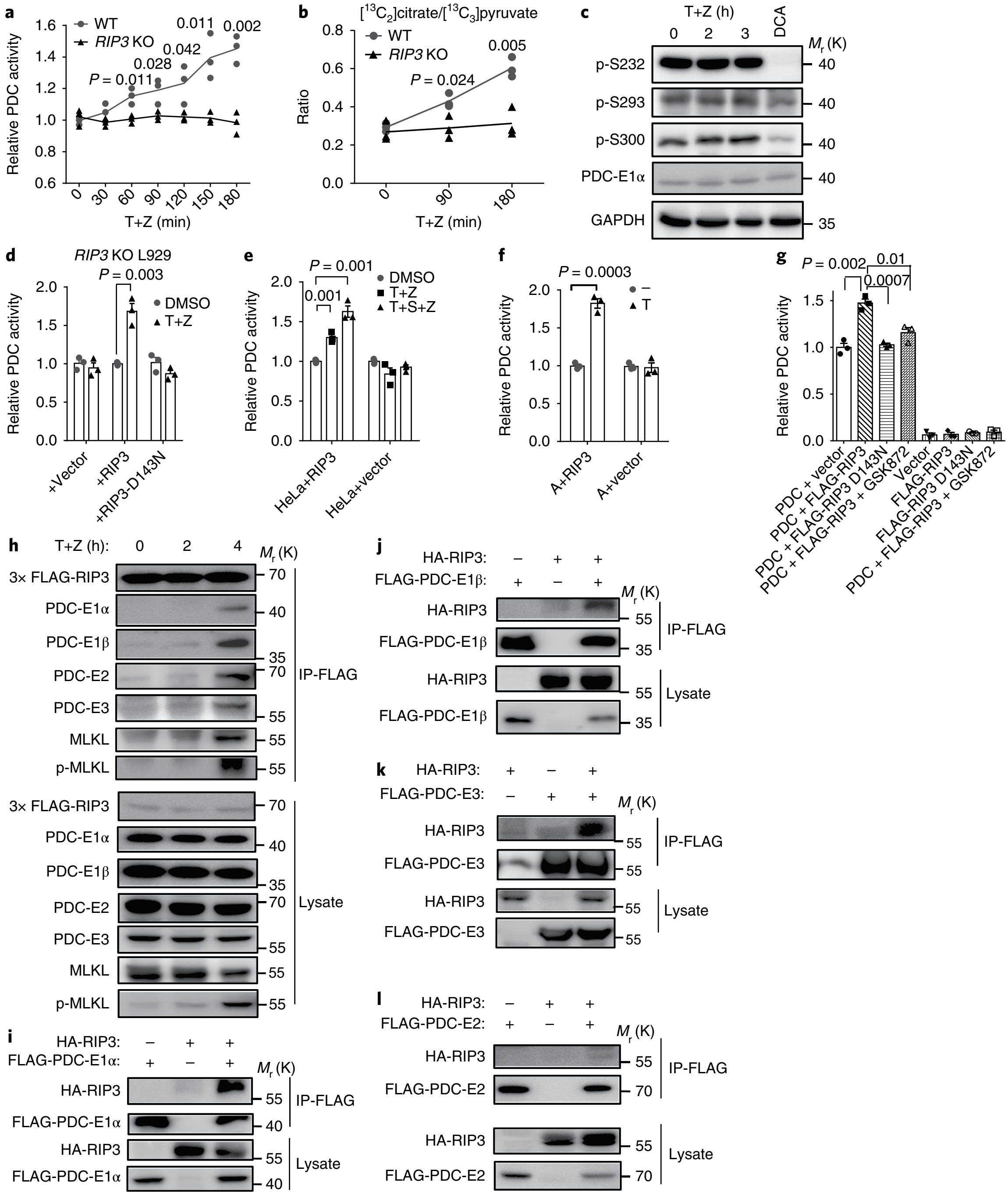

Fig. 5 | RIP3 targets PDC to upregulate aerobic respiration. **a**, WT and *RIP3* KO L929 cells were treated with TNF + zVAD for the indicated periods of time, followed by PDC activity assay. **b**, [U-^{13}C] glucose labelling experiments were performed as described in the Methods. WT and *RIP3* KO L929 cells were treated with TNF + zVAD for the indicated periods of time, followed by GC-MS analysis. The ratio of relative abundance of [$^{13}C_2$]citrate/[$^{13}C_3$] pyruvate indicates PDC activity in intact cells. **c**, L929 cells were treated with TNF + zVAD for the indicated periods of time. The phosphorylation states of PDC-E1α were analysed by immunoblotting. Pyruvate dehydrogenase kinase inhibitor DCA, which inhibits the phosphorylation of PDC-E1, was used as a positive control. **d**, *RIP3* KO L929 cells reconstituted with nothing (vector), RIP3 or RIP3-D143N were treated with or without TNF + zVAD for 3 h followed by PDC activity assay. **e**,**f**, HeLa cells (**e**) or A cells (**f**) expressed with nothing (vector) or RIP3 were treated with indicated stimulus for 5 h, followed by PDC activity assay. **g**, Immunopurified FLAG-RIP3 or FLAG-RIP3 D143N (kinase-dead mutant) from HEK293T were used in the kinase reaction with or without purified PDC for 30 min, followed by PDC activity assay. GSK872 (20 μM, RIP3 kinase inhibitor). **h**, *RIP3* KO L929 cells stable expressing 3× FLAG-RIP3 were treated with TNF + zVAD for the indicated periods of time, and cell lysates were immunoprecipitated with anti-FLAG antibody. Immunocomplexes and cell lysates were analysed by immunoblotting. **i**–**l**, HA-RIP3 and FLAG-PDC-E1α (**i**), FLAG-PDC-E1β (**j**), PDC-E3 (**k**) or PDC-E2 (**l**) were co-expressed in HEK293T cells. At 36 h after transfection, cell lysates were immunoprecipitated with anti-FLAG antibody. Immunocomplexes and cell lysates were analysed by immunoblotting. TNF, 10 ng ml^{-1} (L929), 30 ng ml^{-1} (HeLa, A cell); zVAD, 20 μM; Smac mimetic, 10 μM. For **a**,**b**,**d**–**g**, data are from $n = 3$ independent experiments. Error bars represent mean ± s.e.m. of $n = 3$ independent experiments. Two-tailed Student's *t*-test was applied for *P* values. For **c**,**h**–**l**, results shown are representative of three independent experiments. Statistics source data for this figure are provided in Supplementary Table 1. Uncropped images of blots are shown in Supplementary Fig. 8.

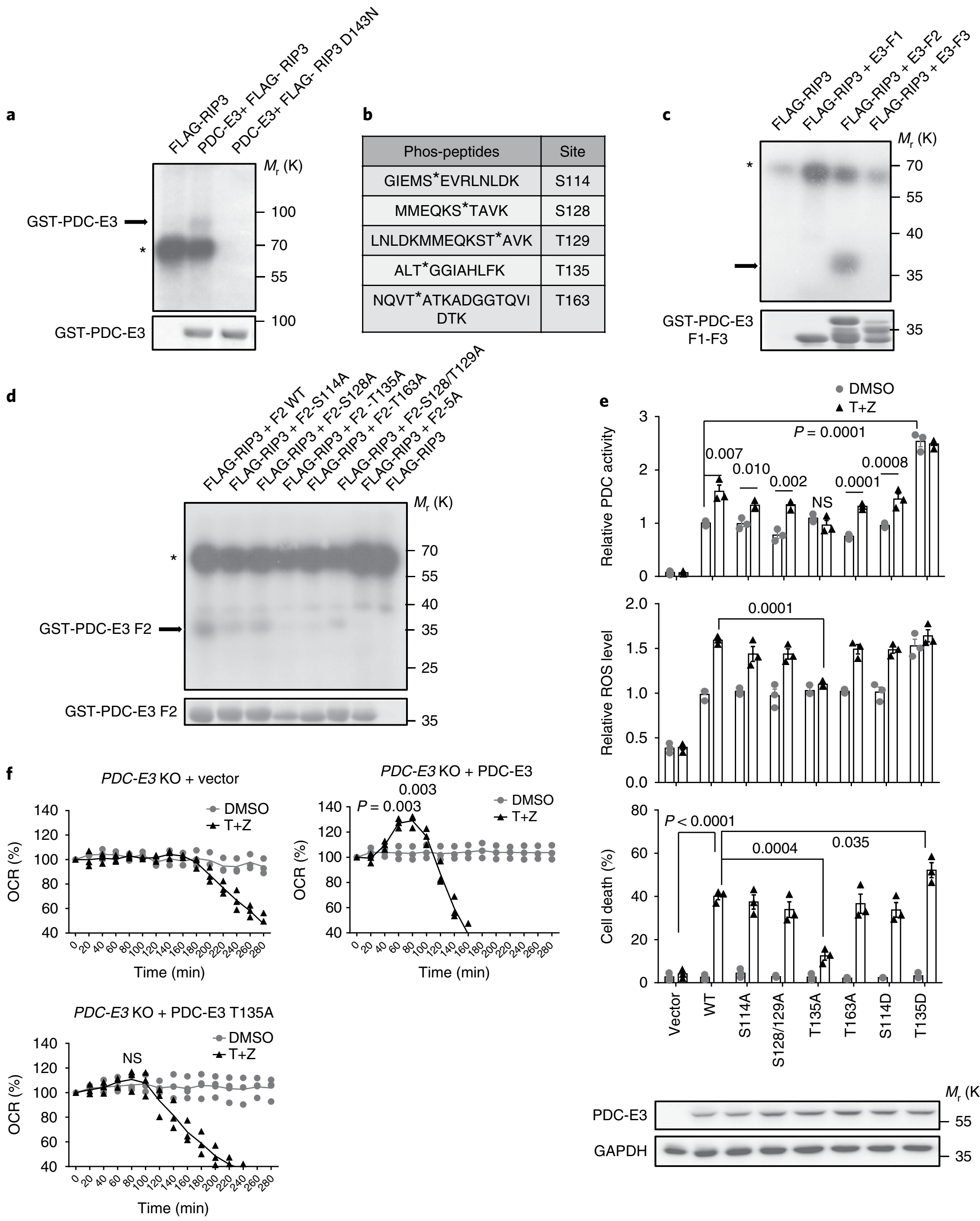

Phos-peptides	Site
GIEMS*EVRLNLDK	S114
MMEQKS*TAVK	S128
LNLDKMMEQKST*AVK	T129
ALT*GGIAHLFK	T135
NQVT*ATKADGGTQVI DTK	T163

Fig. 6 | RIP3 activates PDC by phosphorylating PDC-E3 on T135. **a**, FLAG-RIP3 and FLAG-RIP3 D143N (kinase-dead mutant) immunopurified from HEK293T cells were used in kinase assay with [^{32}P] γ-ATP and PDC-E3 purified from *E. coli*. The X-ray film exposed to SDS–PAGE is shown. Bottom, Coomassie blue staining of PDC-E3. The arrow indicates phosphorylated PDC-E3 and the asterisk indicates RIP3 autophosphorylation. **b**, The same kinase reactions were performed, except that [^{32}P] γ-ATP was not included in the reactions. PDC-E3 was purified and digested with trypsin. The phosphopeptides were enriched by IMAC (immobilized metal ion affinity chromatography), then analysed by MS. Five potential phosphorylation sites of PDC-E3 were identified. **c**, Three peptide fragments of PDC-E3 (F1–F3) were purified from *E. coli* and then used in kinase assay with [^{32}P] γ-ATP and RIP3. Bottom, Coomassie blue staining of PDC-E3 fragments. The arrow indicates the phosphorylated F2 fragment and the asterisk indicates RIP3 autophosphorylation. F1, aa1–85; F2, aa86–171; F3, aa172–256. **d**, WT and indicated mutants of PDC-E3 F2 were purified from *E. coli* and then used in kinase assay with [^{32}P] γ-ATP and FLAG-RIP3. Bottom, Coomassie blue staining of PDC-E3 F2 mutants. The arrow indicates the phosphorylated F2 fragments and the asterisk indicates RIP3 autophosphorylation. **e**, *PDC-E3* KO L929 cells expressed with nothing (vector), WT or indicated mutants of PDC-E3 were treated with or without TNF+zVAD for 2 or 3 h followed by PDC activity assay (3 h), ROS measurement (2 h) and cell viability analysis (3 h). **f**, *PDC-E3* KO L929 cells were expressed with nothing (vector), PDC-E3 or PDC-E3 T135A mutant, followed by OCR measurement over time with the indicated treatments. TNF, 10 ng ml^{-1}; zVAD, 20 μM. For **e**,**f**, data are from $n = 3$ independent experiments. Error bars represent mean ± s.e.m. of $n = 3$ independent experiments. Two-tailed Student's *t*-test was applied for *P* values. NS: no significant difference. For **a**,**b**,**c**,**d**, results shown are representative of three independent experiments. Statistics source data for this figure can be found in Supplementary Table 1. Uncropped images of blots are shown in Supplementary Fig. 8.

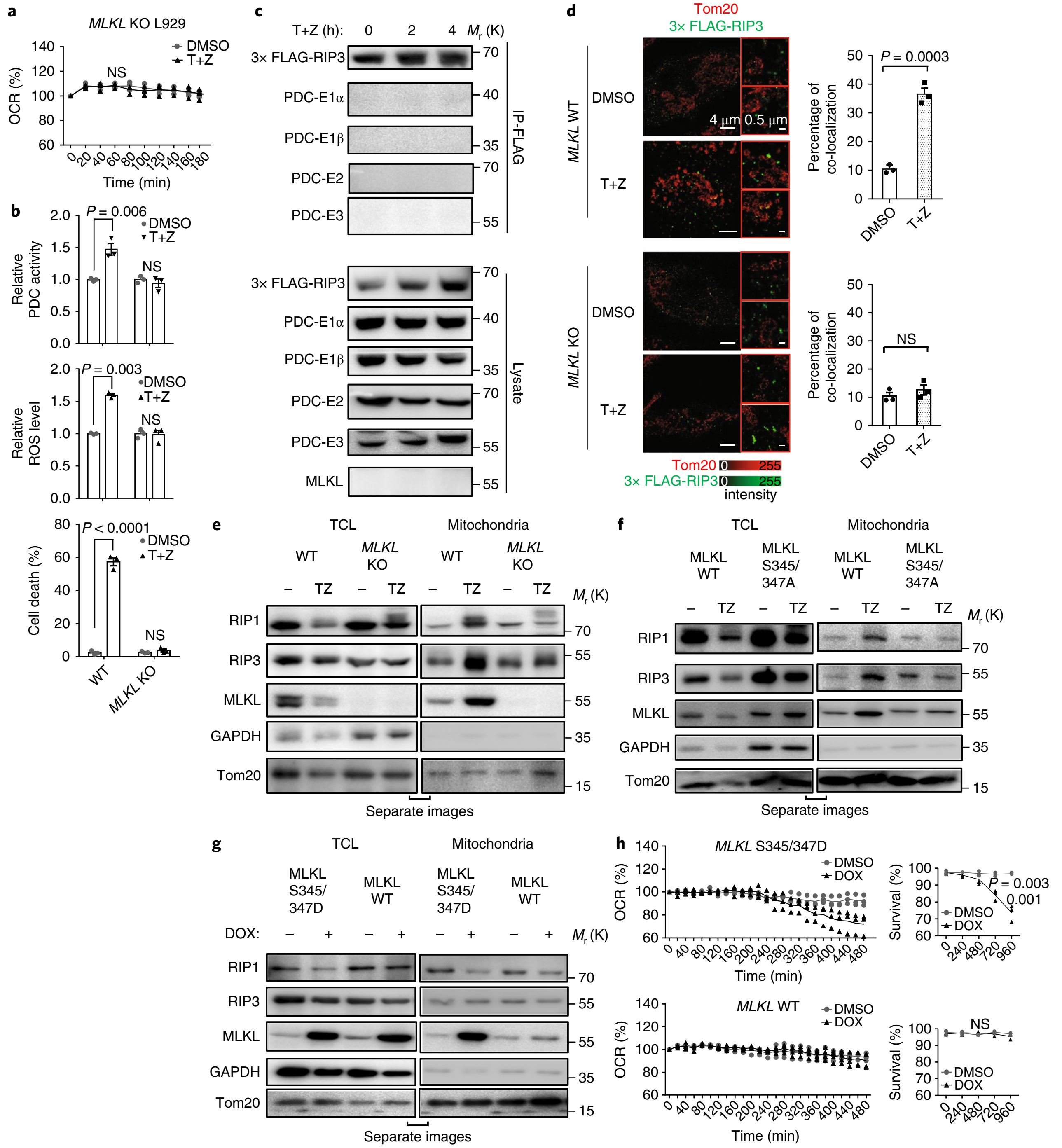

Fig. 7 | MLKL is required for PDC activation. a, OCR of *MLKL* KO L929 cells treated with DMSO or TNF + zVAD were measured over time. **b**, WT and *MLKL* KO L929 cells were treated as indicated for 2 or 3 h followed by PDC activity assay (3 h), ROS measurement (2 h) and cell viability analysis (3 h). **c**, *MLKL* KO L929 cells stable expressing 3× FLAG-RIP3 were treated with TNF + zVAD for the indicated times, then whole-cell extracts were immunoprecipitated with anti-FLAG antibody. Immunocomplexes were analysed by immunoblotting. **d**, Left, *MLKL* WT and KO L929 cells stable expressing 3× FLAG-RIP3 were treated with or without TNF + zVAD for 3 h. Cells were then immunostained for Tom20 (mitochondria, red) and FLAG (green) followed by STORM super-resolution microscopy analysis. Right, percentage of co-localization between mitochondria and RIP3, calculated based on microscopy images (see Methods for details). Scale bars, 4 μm (main images. left) or 0.5 μm (small images, right). **e–g**, WT and *MLKL* KO L929 cells were treated with or without TNF + zVAD for 3 h. In **e**, *MLKL* KO L929 cells reconstituted with MLKL WT or MLKL S345/S347A were treated with or without TNF + zVAD for 3 h. In **f**, *MLKL* KO L929 cells reconstituted with DOX-controlled MLKL WT or MLKL S345/S347D were treated with or without DOX (1 μg ml^{-1}) for 16 h. In **g**, mitochondria of the cells were purified, and indicated protein levels in total cell lysates and mitochondria were analysed by immunoblotting. **h**, *MLKL* KO L929 cells reconstituted with DOX-controlled MLKL WT or MLKL S345/S347D were treated with or without DOX (1 μg ml^{-1}), followed by OCR measurement (left) and cell viability analysis (right). TNF, 10 ng ml^{-1}; zVAD, 20 μM. For **a**,**b**,**d** (right),**h**, data are from $n = 3$ independent experiments. Error bars represent mean ± s.e.m. of $n = 3$ independent experiments. Two-tailed Student's *t*-test was applied for *P* values. NS, no significant difference. For **c**,**d** (left panel),**e**–**g**, data shown are representative of three independent experiments. Samples in **e**–**g** were obtained and processed simultaneously. Statistics source data for this figure are provided in Supplementary Table 1. Uncropped images of blots are shown in Supplementary Fig. 8.

Discussion

We have elucidated the mechanisms of RIP3 to increase aerobic respiration and ROS production. An updated model is shown in Supplementary Fig. 5d. PYGL increases the use of glycogen, which increases pyruvate production. PDC converts pyruvate, from either glycolysis or other sources such as the culture medium, to acetyl-CoA, and triggers the entering of metabolic flux into the TCA cycle. GLUL and GLUD1 play a role in using glutamine as a supplementary substrate for the TCA cycle. Activation of these enzymes has additive effects to aerobic respiration. Activated RIP3 in the necrosome enhances PDC activity by phosphorylating PDC-E3 T135, and plays a major role in increasing aerobic respiration. Because a small percentage of oxygen consumed in respiration is used by the formation of ROS[43], the increase in aerobic respiration is responsible for ROS induction (Supplementary Fig. 5d).

Previous measurements of aerobic respiration in TNF-treated L929 cells were inconsistent[15,16,44]. Different concentrations of digitonin and operation variations might be the cause. The Seahorse XF^e 96 analyser measures OCR in cells without permeabilization, so the data obtained are closer to the true OCR of cells under physiological conditions.

To phosphorylate PDC-E3, a mitochondria matrix localized protein complex[45], RIP3 needs to translocate into mitochondria. The high affinity of MLKL to cardiolipin[11,13], a lipid component of the mitochondrial inner membrane, could be the driving force bringing RIP3 to the inner side of mitochondria.

TNF-induced metabolism was also reflected by an increase in the pool size of TCA cycle intermediates, as both labelled and unlabelled products were increased upon stimulation (Supplementary Fig. 2b, 4b). Pyruvate metabolism contributes more than Gln catabolism (Fig. 6f and Supplementary Fig. 2c). The difference in contribution was also reflected by their effect on ROS induction and necroptosis (Fig. 6e and Supplementary Fig. 2d,e). PYGL-mediated release of glucose-1-phosphate from glycogen might be the major source of pyruvate production, because depletion of pyruvate or glucose from culture medium had a less inhibitory effect on ROS production and necroptosis (Supplementary Fig. 2i,j) when compared with that of PYGL knockdown in our published study[3]. Because of compensation and balance among the metabolism pathways, our data may only provide a rough assessment of the contributions of PYGL, GLUL/GLUD1 and PDC in TNF-induced respiration and ROS production.

Electron leak from a site in complex I (autooxidation of flavin mononucleotide from NADH-dehydrogenase) and a site in complex III (autooxidation of unstable ubisemiquinone) of the respiratory chain can cause mitochondrial superoxide production[46]. A published study has suggested TNF-activated ROS production mainly at the ubisemiquinone site[16]. Apart from this, isolated PDC enzyme could directly produce ROS in vitro under certain conditions[47], so the possibility that TNF-induced PDC activation also directly contributes to ROS generation cannot be excluded.

CypD is known to be required for ischaemia–reperfusion-induced necrosis[48], but CypD and RIP1/RIP3 mediate distinct cell death pathways[49]. Loss of mitochondrial membrane potential was observed in necroptotic cells[50]. Tetramethylrhodamine ethyl ester (TMRE) staining in TNF+zVAD-treated L929 cells showed a slight increase of mitochondrial membrane potential at early time points, and a reduction when cell death became apparent (Supplementary Fig. 6a), consistent with a published study[18]. Since OCR induction occurs much earlier than cell death after TNF+zVAD treatment (Figs. 1a and 2a and Supplementary Fig. 4c), it could not be caused by mitochondrial depolarization. Uncoupling of oxidative respiration with FCCP (carbonyl cyanide-4-(trifluoromethoxy)phenylhydrazone) had no effect on TNF-induced necroptosis in L929 cells[16], and TNF+zVAD still increased OCR after FCCP maximized cell respiration (Supplementary Fig. 6b), confirming that the cause of respiration upregulation is at the sites upstream of the respiration chain. ATP synthase inhibitor oligomycin, which had a minor inhibitory effect on TNF-induced necroptosis[16], inhibited but did not totally block OCR induction (Supplementary Fig. 6b), indicating that TNF+zVAD induced both coupled respiration and oligomycin-insensitive/uncoupled respiration, although the former is the primary effect. Inhibition of complex I by rotenone totally eliminated the induction of OCR, confirming that induction of OCR by TNF resulted from mitochondrial respiration (Supplementary Fig. 6b). Apparently, the respiration in L929 is mostly coupled, but TNF-induced necroptosis does not require it to be coupled or uncoupled.

ROS is not induced by TNF in HT-29 cells, nor is aerobic respiration (Fig. 1f and Supplementary Fig. 1a). The mitochondria in HT-29 cells are phenotypically abnormal, and RIP3 cannot interact with PDC in necroptotic HT-29 cells (Supplementary Fig. 6c,d). HT-29 cells had a low aerobic respiration rate (Supplementary Fig. 6e) and low expression level of all PDC subunits (Supplementary Fig. 6f). In addition, HT-29 lacks mitochondrial pyruvate carrier proteins (MPC1 and MPC2), the crucial transporters of pyruvate from the cell cytosol to the mitochondria matrix[38].

Oxygen levels vary in different parts of the human body[51]. An example is that the partial pressure of oxygen in arterial blood is much higher than that in venous blood[51]. Oxygen depletion (hypoxia) inhibited RIP3-dependent ROS production and necroptosis induced by TNF+zVAD in L929 cells and HeLa+RIP3 cells (Supplementary Fig. 7a,b). Macrophage necroptosis contributes to atherosclerosis development[52] and oxygen depletion inhibited both TNF+zVAD and oxLDL+zVAD-induced necroptosis (Supplementary Fig. 7c,d). Inhibition of ROS induction was correlated with the reduction of necroptosis in the aforementioned experiments (Supplementary Fig. 7e). Hypoxia induces PDK1 expression, which phosphorylates PDC-E1α and inhibits PDC activity[53]. We observed reduced basal PDC activity in all cell types by hypoxia (Supplementary Fig. 7f). The reduced induction of PDC activity in TNF+zVAD- or oxLDL+zVAD-treated hypoxia cells (Supplementary Fig. 7f) could be due to a lack of positive feedback of ROS, because the inhibitory effect of oxygen depletion on basal PDC activity still existed in PDC-E3 T135D- or PDC-E3 T135A-reconstituted cells (Supplementary Fig. 7g), and TNF+zVAD-induced necroptosis was less than with WT L929 cells (Supplementary Fig. 7a,h). Hypoxia could alter the expression levels of many proteins[54], but not RIP1, RIP3 and MLKL (Supplementary Fig. 7i). Thus, environmental oxygen concentration could influence the level of necroptosis induction.

In summary, our work has revealed a mechanism of how RIP3 regulates mitochondrial ROS production. The phosphorylation of PDC-E3 is a previously unknown regulation mechanism of PDC that could enhance aerobic respiration and generate ROS. Because of the importance of aerobic respiration, we believe the phosphorylation-mediated activation of PDC plays a role not only in necroptosis, but also in other biological processes in which oxidative stress participates.

Methods

Methods, including statements of data availability and any associated accession codes and references, are available at https://doi.org/10.1038/s41556-017-0022-y.

Received: 9 September 2016; Accepted: 5 December 2017;

References

1. Laster, S. M., Wood, J. G. & Gooding, L. R. Tumor necrosis factor can induce both apoptic and necrotic forms of cell lysis. *J. Immunol.* **141**, 2629–2634 (1988).
2. Kerr, J. F., Wyllie, A. H. & Currie, A. R. Apoptosis: a basic biological phenomenon with wide-ranging implications in tissue kinetics. *Br. J. Cancer* **26**, 239–257 (1972).

3. Zhang, D. W. et al. RIP3, an energy metabolism regulator that switches TNF-induced cell death from apoptosis to necrosis. *Science* **325**, 332–336 (2009).
4. He, S. et al. Receptor interacting protein kinase-3 determines cellular necrotic response to TNF-α. *Cell* **137**, 1100–1111 (2009).
5. Cho, Y. S. et al. Phosphorylation-driven assembly of the RIP1-RIP3 complex regulates programmed necrosis and virus-induced inflammation. *Cell* **137**, 1112–1123 (2009).
6. Wu, X. N. et al. Distinct roles of RIP1-RIP3 hetero- and RIP3-RIP3 homo-interaction in mediating necroptosis. *Cell. Death Differ.* **21**, 1709–1720 (2014).
7. Orozco, S. et al. RIPK1 both positively and negatively regulates RIPK3 oligomerization and necroptosis. *Cell. Death Differ.* **21**, 1511–1521 (2014).
8. Chen, W. et al. Ppm1b negatively regulates necroptosis through dephosphorylating Rip3. *Nat. Cell. Biol.* **17**, 434–444 (2015).
9. Sun, L. et al. Mixed lineage kinase domain-like protein mediates necrosis signaling downstream of RIP3 kinase. *Cell* **148**, 213–227 (2012).
10. Zhao, J. et al. Mixed lineage kinase domain-like is a key receptor interacting protein 3 downstream component of TNF-induced necrosis. *Proc. Natl. Acad. Sci. USA* **109**, 5322–5327 (2012).
11. Wang, H. et al. Mixed lineage kinase domain-like protein MLKL causes necrotic membrane disruption upon phosphorylation by RIP3. *Mol. Cell.* **54**, 133–146 (2014).
12. Chen, X. et al. Translocation of mixed lineage kinase domain-like protein to plasma membrane leads to necrotic cell death. *Cell. Res.* **24**, 105–121 (2014).
13. Dondelinger, Y. et al. MLKL compromises plasma membrane integrity by binding to phosphatidylinositol phosphates. *Cell. Rep.* **7**, 971–981 (2014).
14. Cai, Z. et al. Plasma membrane translocation of trimerized MLKL protein is required for TNF-induced necroptosis. *Nat. Cell. Biol.* **16**, 55–65 (2014).
15. Goossens, V. et al. Redox regulation of TNF signaling. *BioFactors* **10**, 145–156 (1999).
16. Schulze-Osthoff, K. et al. Cytotoxic activity of tumor necrosis factor is mediated by early damage of mitochondrial functions. Evidence for the involvement of mitochondrial radical generation. *J. Biol. Chem.* **267**, 5317–5323 (1992).
17. Schulze-Osthoff, K., Beyaert, R., Vandevoorde, V., Haegeman, G. & Fiers, W. Depletion of the mitochondrial electron transport abrogates the cytotoxic and gene-inductive effects of TNF. *EMBO J.* **12**, 3095–3104 (1993).
18. Tait, S. W. et al. Widespread mitochondrial depletion via mitophagy does not compromise necroptosis. *Cell. Rep.* **5**, 878–885 (2013).
19. Schenk, B. & Fulda, S. Reactive oxygen species regulate Smac mimetic/TNFα -induced necroptotic signaling and cell death. *Oncogene* **34**, 5796–5806 (2015).
20. Zhang, Y. et al. RIP1 autophosphorylation is promoted by mitochondrial ROS and is essential for RIP3 recruitment into necrosome. *Nat. Commun.* **8**, 14329 (2017).
21. Kim, Y. S., Morgan, M. J., Choksi, S. & Liu, Z. G. TNF-induced activation of the Nox1 NADPH oxidase and its role in the induction of necrotic cell death. *Mol. Cell.* **26**, 675–687 (2007).
22. Turrens, J. F., Freeman, B. A., Levitt, J. G. & Crapo, J. D. The effect of hyperoxia on superoxide production by lung submitochondrial particles. *Arch. Biochem. Biophys.* **217**, 401–410 (1982).
23. Turrens, J. F. Mitochondrial formation of reactive oxygen species. *J. Physiol.* **552**, 335–344 (2003).
24. Jastroch, M., Divakaruni, A. S., Mookerjee, S., Treberg, J. R. & Brand, M. D. Mitochondrial proton and electron leaks. *Essays Biochem.* **47**, 53–67 (2010).
25. Harris, R. A., Bowker-Kinley, M. M., Huang, B. & Wu, P. Regulation of the activity of the pyruvate dehydrogenase complex. *Adv. Enzym. Reg.* **42**, 249–259 (2002).
26. Roche, T. E. et al. Distinct regulatory properties of pyruvate dehydrogenase kinase and phosphatase isoforms. *Prog. Nucleic Acid. Res. Mol. Biol.* **70**, 33–75 (2001).
27. Kaplon, J. et al. A key role for mitochondrial gatekeeper pyruvate dehydrogenase in oncogene-induced senescence. *Nature* **498**, 109–112 (2013).
28. Hitosugi, T. et al. Tyrosine phosphorylation of mitochondrial pyruvate dehydrogenase kinase 1 is important for cancer metabolism. *Mol. Cell.* **44**, 864–877 (2011).
29. Temkin, V., Huang, Q., Liu, H., Osada, H. & Pope, R. M. Inhibition of ADP/ATP exchange in receptor-interacting protein-mediated necrosis. *Mol. Cell. Biol.* **26**, 2215–2225 (2006).
30. Hanson, G. T. et al. Investigating mitochondrial redox potential with redox-sensitive green fluorescent protein indicators. *J. Biol. Chem.* **279**, 13044–13053 (2004).
31. Narendra, D., Tanaka, A., Suen, D. F. & Youle, R. J. Parkin is recruited selectively to impaired mitochondria and promotes their autophagy. *J. Cell. Biol.* **183**, 795–803 (2008).
32. Festjens, N. et al. Butylated hydroxyanisole is more than a reactive oxygen species scavenger. *Cell. Death Differ.* **13**, 166–169 (2006).
33. Goossens, V., Grooten, J. & Fiers, W. The oxidative metabolism of glutamine. A modulator of reactive oxygen intermediate-mediated cytotoxicity of tumor necrosis factor in L929 fibrosarcoma cells. *J. Biol. Chem.* **271**, 192–196 (1996).
34. Zachar, Z. et al. Non-redox-active lipoate derivates disrupt cancer cell mitochondrial metabolism and are potent anticancer agents in vivo. *J. Mol. Med.* **89**, 1137–1148 (2011).
35. El Sayed, S. M. et al. Safety and outcome of treatment of metastatic melanoma using 3-bromopyruvate: a concise literature review and case study. *Chin. J. Cancer* **33**, 356–364 (2014).
36. Deck, L. M. et al. Selective inhibitors of human lactate dehydrogenases and lactate dehydrogenase from the malarial parasite *Plasmodium falciparum*. *J. Med. Chem.* **41**, 3879–3887 (1998).
37. Hiromasa, Y., Fujisawa, T., Aso, Y. & Roche, T. E. Organization of the cores of the mammalian pyruvate dehydrogenase complex formed by E2 and E2 plus the E3-binding protein and their capacities to bind the E1 and E3 components. *J. Biol. Chem.* **279**, 6921–6933 (2004).
38. Schell, J. C. et al. A role for the mitochondrial pyruvate carrier as a repressor of the Warburg effect and colon cancer cell growth. *Mol. Cell.* **56**, 400–413 (2014).
39. Thapa, R. J. et al. Interferon-induced RIP1/RIP3-mediated necrosis requires PKR and is licensed by FADD and caspases. *Proc. Natl. Acad. Sci. USA* **110**, E3109–3118 (2013).
40. Zhong, C. Q. et al. Quantitative phosphoproteomic analysis of RIP3-dependent protein phosphorylation in the course of TNF-induced necroptosis. *Proteomics* **14**, 713–724 (2014).
41. Grassian, A. R., Metallo, C. M., Coloff, J. L., Stephanopoulos, G. & Brugge, J. S. Erk regulation of pyruvate dehydrogenase flux through PDK4 modulates cell proliferation. *Genes. Dev.* **25**, 1716–1733 (2011).
42. Rodriguez, D. A. et al. Characterization of RIPK3-mediated phosphorylation of the activation loop of MLKL during necroptosis. *Cell. Death Differ.* **23**, 76–88 (2016).
43. Boveris, A. & Chance, B. The mitochondrial generation of hydrogen peroxide. General properties and effect of hyperbaric oxygen. *Biochem. J.* **134**, 707–716 (1973).
44. Hennet, T., Richter, C. & Peterhans, E. Tumour necrosis factor-alpha induces superoxide anion generation in mitochondria of L929 cells. *Biochem. J.* **289**, 587–592 (1993).
45. Joplin, R. et al. Subcellular localization of pyruvate dehydrogenase dihydrolipoamide acetyltransferase in human intrahepatic biliary epithelial cells. *J. Pathol.* **176**, 381–390 (1995).
46. Turrens, J. F. & Boveris, A. Generation of superoxide anion by the NADH dehydrogenase of bovine heart mitochondria. *Biochem. J.* **191**, 421–427 (1980).
47. Starkov, A. A. et al. Mitochondrial alpha-ketoglutarate dehydrogenase complex generates reactive oxygen species. *J. Neurosci.* **24**, 7779–7788 (2004).
48. Nakagawa, T. et al. Cyclophilin D-dependent mitochondrial permeability transition regulates some necrotic but not apoptotic cell death. *Nature* **434**, 652–658 (2005).
49. Linkermann, A. et al. Two independent pathways of regulated necrosis mediate ischemia–reperfusion injury. *Proc. Natl. Acad. Sci. USA* **110**, 12024–12029 (2013).
50. Baines, C. P. et al. Loss of cyclophilin D reveals a critical role for mitochondrial permeability transition in cell death. *Nature* **434**, 658–662 (2005).
51. Malatesha, G., Singh, N. K., Bharija, A., Rehani, B. & Goel, A. Comparison of arterial and venous pH, bicarbonate, PCO_2 and PO_2 in initial emergency department assessment. *Emerg. Med. J.* **24**, 569–571 (2007).
52. Lin, J. et al. A role of RIP3-mediated macrophage necrosis in atherosclerosis development. *Cell. Rep.* **3**, 200–210 (2013).
53. Kim, J. W., Tchernyshyov, I., Semenza, G. L. & Dang, C. V. HIF-1-mediated expression of pyruvate dehydrogenase kinase: a metabolic switch required for cellular adaptation to hypoxia. *Cell. Metab.* **3**, 177–185 (2006).
54. Moriwaki, K., Bertin, J., Gough, P. J., Orlowski, G. M. & Chan, F. K. Differential roles of RIPK1 and RIPK3 in TNF-induced necroptosis and chemotherapeutic agent-induced cell death. *Cell. Death Dis.* **6**, e1636 (2015).

Acknowledgements

This work was supported by the National Natural Science Foundation of China (91429301), the National Basic Research Program of China (973 Program;

2015CB553800 and 2014CB541804), the National Natural Science Foundation of China (31420103910, 31330047 and 81788104), the 111 Project (B12001), the National Science Foundation of China for Fostering Talents in Basic Research (J1310027) and the Open Research Fund of State Key Laboratory of Cellular Stress Biology, Xiamen University.

Author contributions

Z.Y. and J.H. conceived and designed the experiments. Z.Y., Y.W., Y.Z. and X.C. performed the experiments. X.H. and C.-Q.Z. performed the GC-MS and MS experiments and analysed the obtained results. H.N., Y.L. and J.W. helped to prepare cell lines for the study. S.Z. and D.Z. provided technical support. Z.Y. and J.H. interpreted the data and wrote the paper.

Competing interests

The authors declare no competing financial interests.

Additional information

Supplementary information is available for this paper at https://doi.org/10.1038/s41556-017-0022-y.

Reprints and permissions information is available at www.nature.com/reprints.

Correspondence and requests for materials should be addressed to J.H.

Methods

Cell lines and cell culture. L929, HEK293T, HeLa, HT-29 and RAW 264.7 cells were obtained from ATCC. An L929 subline that is insensitive to zVAD-induced autophagic cell death was used in our experiment. RIP1 KO, RIP3 KO, MLKL KO and 3× FLAG RIP3-reconstituted RIP3 KO L929 cells were established as described in ref. [55]. RIP3 KO RAW 264.7 cells, PDC-E1α KO, PDC-E1β KO and PDC-E3 KO L929 cells were generated using CRISPR/Cas9 or the TALEN gene editing technique. The KO cells were determined by sequencing targeted loci and western blot. RIP3 WT and KO MEFs were isolated from mouse embryos at 13.5 days post conception(dpc). Male and female RIP3$^{+/-}$ heterozygous mice (6–8 weeks old, C57BL/6 strain) were crossed to obtain embryos to generate RIP3 WT/KO MEFs and WT/KO mice to harvest peritoneal macrophages. MEFs were isolated from mouse embryos at 13.5 dpc. Peritoneal macrophages were elicited by thioglycollate medium. We complied with all relevant ethical regulations, and all animal experimental protocols were approved by the institutional Animal Care and Use Committee at Xiamen University. The NIH 3T3-A cell line has been described in our previous work[56]. HT-29 cells were cultured in McCoy's 5A culture medium (Invitrogen), and other cells were cultured in DMEM unless otherwise indicated. All media were supplemented with 10% FBS, 2 mM L-glutamine, 100 IU penicillin and 100 mg ml^{-1} streptomycin at 37 °C in a humidified incubator containing 5% CO$_2$ unless otherwise indicated. All cell lines were authenticated by morphology and DNA sequencing, and were repeatedly tested to be mycoplasma-free, as judged by the MycoAlert Mycoplasma Detection Kit (Lonza, LT-07).

Reagents and antibodies. Mouse and human TNF-α was purchased from eBioscience. zVAD was obtained from Calbiochem, and Smac mimetic (SM-164) was from APExBIO. Propidium iodide (PI), 3-BrPA, BHA and purified PDC were purchased from Sigma. All dyes and MitoSOX were provided by Invitrogen. CPI-613 (S2776) was purchased from Selleck. oxLDL was purchased from Unionbiol.

Rabbit-anti-human RIP3 antibody, abcam-ab152130, 1:1,000 dilution; rabbit-anti-p-PDC-E1α(S293) antibody (EPR12200), abcam-ab177461, 1:1,000 dilution; rabbit-anti-p-PDC-E1α(S293) antibody, abcam-ab115343, 1:1,000 dilution; rabbit-anti-p-PDC-E1α(S300) antibody, abcam-ab114345, 1:1,000 dilution; rabbit-anti-tom20(FL145) antibody, santa cruz-sc11415, 1:500 dilution; mouse-anti-GAPDH(6C5) antibody, santa cruz-sc32233, 1:500 dilution; mouse-anti-FLAG antibody, sigma-F1804, 1:1,000 dilution; mouse-anti-β-actin(AC-15) antibody, sigma-A1978, 1:10,000 dilution; mouse-anti-RIP1 antibody, BD biosciences-610456, 1:1,000 dilution; rabbit-anti-mRIP3 antibody, raised from rabbit by using *E. coli*-expressed GST-RIP3 (287-387 amino acid), 1:1,000 dilution; rabbit-anti-PDC-E1α antibody, Proteintech-18068-1-AP, 1:1,000 dilution; rabbit-anti-PDC-E1β antibody, Proteintech-14744-1-AP, 1:1,000 dilution; rabbit-anti-PDC-E2 antibody, Proteintech-13426-1-AP, 1:500 dilution; rabbit-anti-PDC-E3 antibody, Proteintech-16431-1-AP, 1:1,000 dilution; rabbit-anti-LDHA antibody, Proteintech-19987-1-AP, 1:500 dilution.

Constructs. For mammalian cells expression, full-length or mutated cDNAs of PDC-E1α, PDC-E1β, PDC-E2, PDC-E3 were PCR-amplified from a human cDNA library. For protein preparation in *E. coli*, cDNAs of PDC-E1α, PDC-E1β, PDC-E2, PDC-E3 and PDC-E3 mutants were cloned into vector pGEX-4T1-GST. RIP3 and RIP3-D143N cDNAs were also cloned into the pBOB vector. All plasmids were verified by DNA sequencing. Details of the sequences are available upon request. Primers sequences used to amplify these genes were:

PDC-E1α-F: 5′-agagaattcggatccatgaggaagatgctcgccgc-3′;
PDC-E1α-R: 5′-cttccatggctcgagcccgggttaactgactgacttaaacttgatccac-3′;
PDC-E1β-F: 5′-agagaattcggatccatggcggcggtgtctggctt-3′;
PDC-E1β-R: 5′-cttccatggctcgagcccgggctaaatatttaatgttttctttattgcaaatatg-3′;
PDC-E2-F: 5′-agagaattcggatccatgtggcgcgtctgtgcgc-3′;
PDC-E2-R: 5′-cttccatggctcgagcccgggttacaacaacatagtgataggtttttcaag-3′;
PDC-E3-F: 5′-agagaattcggatccatgcagagctggagtcgtgt-3′;
PDC-E3-R: 5′-cttccatggctcgagcccgggaaagttgattgatttgccaaatgacg-3′;
RIP3-F: 5′-agagaattcggatccatgtcttctgtcaagttatg-3′;
RIP3-R: 5′-cttccatggctcgagcccgggctacttgtggaagggctgcca-3′.

Cell viability assay. The cell viabilities of L929, NIH 3T3-A and RAW264.7 cells were determined by flow cytometry with two parameters: cell size and plasma membrane integrity. Cells were trypsinized and collected, centrifuged, washed once with PBS, and resuspended in DMEM containing 5 µg ml^{-1} PI. The levels of PI incorporation were quantified with a FACScan flow cytometer. Peritoneal macrophage cell death was measured by PI staining as previously described[57].

Cell metabolism analysis. Aerobic respiration was monitored in real time with the Seahorse Bioscience Extracellular Flux Analyzer (XF96; Seahorse Bioscience) by measuring OCR as described in ref. [58]. Briefly, 8,000 cells (each well) were cultured overnight in custom XF96 microplates. Before measurement, cells were washed and immersed in fresh medium for 1 h. The injection and assay procedure was set as 'Mix-03:00, wait-00:00, Measurment-03:00' for three cycles, followed by injection from reagent port A. The measurement cycle was set as 'Mix-03:00, wait-14:00, Measurment-03:00' for 30 cycles. After measurement, cells were trypsin-digested and counted for cell number if the exact value of OCR was needed. Assay medium was unbuffered DMEM (without sodium hydrogen carbonate, without serum, pH = 7.4).

PDC activity assay. Cells were cultured in 10 cm tissue culture dishes in normal DMEM. Indicated stimuli were added when cells were ~90% confluent. After treatment, each dish was washed with PBS three times to remove dead cells. Cells were then collected and PDC activity was measured using a PDH enzyme activity microplate assay kit (abcam ab109902-MSP18). Briefly, 150 µl PBS with 1/9 volume detergent was added into each 1.5 ml tube with cells collected from one 10 cm dish. The tubes were kept on ice for 10 min after gentle mixing. Tubes were centrifuged at 1,000*g* for 10 min and the supernatant was transferred into a new tube. Protein concentration was measured with BCA and 200 µg protein per well with 20 × sample buffer was loaded into the 96-well assay plate and kept at room temperature for 4 h. Reaction buffer was mixed with 100 × coupler, 100 × dye, 20 × reagent mix and 20 × sample buffer. Liquid in the assay plate wells was removed and washed twice with 1 × stabilizer. 200 µl reaction buffer was added into each well, and absorbance was measured at 450 nm every 30 s for 30 cycles with a microplate reader. The slope of the kinetic cure was calculated to indicate PDC activity. The in vitro PDC activation experiment was performed by using PDC purified from porcine heart (SIGMA-P7032) and FLAG-RIP3 or FLAG-RIP3 D143N protein from HEK293T cells.

In vitro PDC activation experiment. PDC solution (1 µl, 0.1–1.0 units per mg protein) and 5 µl FLAG-RIP3 or FLAG-RIP3 D143N beads were incubated with 100 µM cold ATP in kinase buffer at 30 °C for 30 min followed by PDC activity assay with the standard protocol (details shown above).

Correlation analysis between BHA-mediated inhibition of cell death and maximum increase in OCR in different cell lines. Cells were pretreated with or without BHA (100 µM) for 1 h and then treated with TNF+zVAD (N cell, A cell+RIP3, HeLa+RIP3, macrophage) or TNF+Smac mimetic+zVAD (RAW264.7, HT-29). Cell death was analysed when most of the cells died in the samples without BHA pretreatment, and cell death (percentage) differences between cells pretreated with or without BHA were recorded as BHA-mediated inhibition of cell death. OCRs of these cell lines with indicated treatments were measured over time, and the maximum increases in OCR (percentage) were recorded and analysed with BHA-mediated inhibition of cell death for correlation by linear regression analysis with GraphPad Prism.

In vitro kinase assay. GST-tagged PDC-E1α, PDC-E1β, PDC-E2, PDC-E3 and PDC-E3 mutants were expressed and purified form *E. coli*. WT FLAG-RIP3 and FLAG-RIP3 D143N proteins were immunoprecipitated using anti-FLAG beads from cell lysates of transfected 293T cells (15 cm plate). After washing three times with kinase buffer (25 mM Tris, pH 7.5, 10 mM MgCl$_2$, 2 mM dithiothreitol (DTT), 5 mM β-glycerophosphate, 0.1 mM Na$_3$VO$_4$), the beads were suspended in 20 µl of kinase buffer. GST-tagged protein, FLAG-RIP3 beads, 10 µM cold ATP and 2 µCi of [γ-^{32}P] ATP were added to initiate the reaction. Samples were incubated at 30 °C for 30 min and then subjected to SDS–PAGE followed by autoradiography.

Lentivirus preparation and infection. For lentivirus production, HEK293T cells were transfected with lentiviral vectors and virus-packing plasmids by calcium phosphate transfection. The virus-containing medium was collected 48–60 h later and added to cells with 10 µg ml^{-1} of polybrene, then centrifuged at 2,500 r.p.m. for 30 min. Infectious medium was changed with fresh medium 12–24 h later.

Immunoprecipitation and western blotting. Immunoprecipitations were performed using anti-Flag M2 beads as described[56]. Western blotting of the cell lysates and immunoprecipitates was performed using anti-RIP3, anti-Flag, anti-HA and other antibodies, as indicated. Three independent experiments were performed to assess reproducibility.

Measurement of ROS by MitoSOX. Cells were cultured in 12-well plates and treated with the indicated stimulants. After treatment, the culture medium was removed and the cells were washed with PBS and then incubated for 20 min at 37 °C with MitoSOX at a final concentration of 2.5 µM in Hank's balanced-salt solution (HBSS). Cells were washed with warm PBS, removed from the plates with trypsin-EDTA, pelleted at 1,500 r.p.m. for 3 min, resuspended in cold HBSS, and analysed by flow cytometry.

Investigation of mitochondrial redox potential by mito-roGFP. Mitochondrial roGFP2 expressing plasmid (#49437) was purchased from Addgene and subcloned into lentivirus-packing vector pLV. WT/*RIP3* KO L929 and HeLa+RIP3/vector cells were infected with lentivirus encoding mito-roGFP2 to get stable cell lines. The detailed experimental procedures have been described previously[59,60]. Briefly, cells were cultured in glass-bottomed dishes and maintained at 37 °C using an open perfusion microincubator (Zeiss). After TNF+zVAD treatment, time series of dual excitation images (405 nm/488 nm excitation, 500–540 nm emission) were taken by Zeiss LSM 780 laser scanning confocal microscope with a ×63/1.40 NA oil objective using identical settings. Data were analysed with MacBiophotonics

ImageJ software. Fluorescence excitation ratios (405 nm/488 nm) were obtained by dividing integrated intensities obtained from manually selected portions of the imaged intact whole cells ($n=13$ (L929 WT), 13 (L929 RIP3 KO) or 11 (HeLa+RIP3/vector)) collected using 405 nm and 488 nm excitation after appropriate background correction. Background correction was performed by subtracting the intensity of a nearby cell-free region from the signal of the imaged cell.

Measurement of mitochondrial potential by TMRE staining. Cells were cultured in 12-well plates and treated with TNF+zVAD for the indicated periods of time. After treatment, TMRE was added to the culture medium at a final concentration of 100 nM and then incubated for 20 min at 37 °C. Cells were then washed with PBS, removed from the plates with trypsin-EDTA, pelleted at 1,500 r.p.m. for 3 min, resuspended in PBS and analysed by flow cytometry.

CRISPR/Cas9 and TALEN gene editing techniques. Details of CRISPR/Cas9 and TALEN gene editing techniques have been described previously[61–63]. The Cas9 targeting sequences were as follows:

PDC-E3-site 1: 5′-GTTGTTCACGTCAATGGATT-3′;
PDC-E3-site 2: 5′-GTTACAGCTACAAAAGCCGA-3′.
The TALEN targeting sites are as follows:
PDC-E1α: 5′-TAGGCAAGCCGAGTGCT-3′ and 5′-ATTTTGCAAATGATGCTA-3′;
PDC-E1β: 5′-TAGGTTAGCAGAGGCCT-3′ and 5′-ACAAGAGGATCATCGACA-3′;
RIP3: 5′-CTAACATTCTGCTGGA-3′ and 5′-TGTAGATGGACTAACC-3′.

RNA interference. All lentiviral-shRNAs were constructed into pLV-H1-EF1α-puro vector following the manufacturer's instruction (Biosettia). The indicated shRNA target sequences were

PDC-E1α-1: 5′-AGGTTGTGCTAAAGGGAAA-3′;
PDC-E1α-2: 5′-TGCAAGTGTTGAAGAATTA-3′;
LDHA: 5′-CATGATTAAGGGTCTCTAT-3′.

^{13}C metabolite labelling and gas chromatography–mass spectrometry analysis. ^{13}C metabolism labelling experiments were performed as described previously[64]. Cells were cultured in normal DMEM medium in 10 cm tissue culture dishes. Metabolic experiments were performed when cells were ~90% confluent. Medium for ^{13}C glucose labelling experiments contained 10 mM [U-^{13}C] glucose (Cambridge Isotope Labs) and 2 mM unlabelled glutamine. Medium for ^{13}C glutamine labelling experiments contained 10 mM unlabelled glucose and 2 mM [U-^{13}C] glutamine (Cambridge Isotope Labs). Medium containing ^{13}C-labelled nutrients did not contain sodium pyruvate. Each dish of cells was washed in PBS and replenished with the labelling medium. Cells were then treated with TNF+zVAD for the indicated periods of time. After treatment, each dish of cells was washed three times with PBS, then 80% pre-cold methanol with 1 mM internal standard ribitol was added to cells. At the same time, parallel dishes were used to count cell numbers using a Countstar IC1000 cell counter. Metabolite extractions were then lyophilized in 1.5 ml glass bottles and oximated with 20 mg ml^{-1} methoxyamine hydrochloride in pyridine at 70 °C for 60–90 min. Derivatized samples with 20 µl *N*-methyl-*N*-(*tert*-butyldimethylsilyl) trifluoroacetamide in 80 µl pyridine at 30 °C for 30–60 min. After filtration, 2 µl of samples was injected for gas chromatography–mass spectrometry (GC-MS) analysis using an Agilent 6890-5973 GC-MS system with a HP-5MS column (30 m 0.25 mm 0.25 µm). GC oven temperature was programmed from 60 °C to 180 °C at 5 °C min^{-1} and from 180 °C to 260 °C at 10 °C min^{-1}. The flow rate of carrier gas was set at 1 ml min^{-1}. The mass spectrometer was operated in the electron impact (EI) mode at 70 eV. Relative metabolite abundances were determined by normalizing the abundances of each metabolite to the internal standard and to cell number. The incorporation of ^{13}C atoms are denoted as $m+n$, where n is the number of ^{13}C atoms.

MS analysis. The purified GST-PDC-E3 proteins were incubated with FLAG-RIP3 or FLAG-RIP3 D143N (kinase dead) proteins at 30 °C in kinase buffer for 30 min and the reactions were subjected to SDS–PAGE. Bands responding to GST-PDC-E3 proteins were excised and subjected to in-gel digestion. Briefly, the gels were cut into 1 mm^3 cubes, and de-stained with 50 mM NH$_4$HCO$_3$/50% acetonitrile. The proteins were reduced using 25 mM DTT/50 mM NH$_4$HCO$_3$ at 56 °C for 20 min and cysteines were alkylated using 55 mM iodoacetamide/50 mM NH$_4$HCO$_3$ for 20 min at room temperature in the dark. After adding 200 ng trypsin, digestions were performed at 37 °C overnight. The peptides were de-salted with ziptips followed by IMAC-Fe^{3+} enrichment as previously described[65]. Peptides were dissolved in 50 µl 1% acetic acid/60% acetonitrile and incubated with 5 µl IMAC beads while shaking for 30 min at room temperature. After washing the IMAC beads with 50 µl 1% acetic acid/60% acetonitrile twice, phosphopeptides were eluted with 5% NH$_3$.H$_2$O. Phophopeptides were analysed on a TripleTOF 5600 (AB Sciex) mass spectrometer coupled to a NanoLC Ultra 2D Plus (Eksigent) HPLC system. Peptides first bound to a 5 mm × 500 µm trap column packed with Zorbax C18 5-µm 200-Å resin using 0.1% (vol/vol) formic acid/2% acetonitrile in H$_2$O at 10 µl min^{-1} for 5 min, and then separated using a 60 min gradient of 2–35% buffer B (buffer A: 0.1% (vol/vol) formic acid, 5% DMSO in H$_2$O, buffer B: 0.1% (vol/vol) formic acid, 5% DMSO in acetonitrile) on a 15 cm × 75 µm in-house pulled emitter-integrated column packed with Magic C18 AQ 3-µm 200 Å resin. The acquired wiff files were searched with Maxquant version 1.5 against the full non-redundant, canonical mouse genome as annotated by UniprotKB/Swiss-Prot (downloaded in September 2014). Database search parameters were set as follows: carbamidomethylation (C) was set as fixed modification; methionine oxidation and phosphorylation on STY were set as variable modification; semi-tryptic peptides and peptides with up to two missed cleavages were allowed. All identified phosphopeptides of PDC-E3 proteins were selected and manually checked. MS data have been deposited in ProteomeXchange with the primary accession code PXD008004.

Structured illumination microscopy. For fixed-cell imaging, cells were fixed with freshly prepared 4% paraformaldehyde (PFA) in PBS and then permeabilized in 0.2% Triton X-100/PBS, blocked with 3% BSA in PBS, stained with anti-Flag (rabbit, 1:200, Sigma) or anti-Tom20 (mouse, 1:100, Santa Cruz) and labelled with goat anti-mouse or rabbit AlexaFluor 488 (1:1,000, Invitrogen) or mouse AlexaFluor 568 (1:1,000, Invitrogen). Cells were counterstained with Hoechst to visualize the nuclei. All images were captured and processed using identical settings in a structured illumination microscopy GE DeltaVision OMX V4. Duplicate cultures were examined and similar results were obtained in at least three independent experiments.

Stochastic optical reconstruction microscopy and RIP3-mitochondria co-localization analysis. STORM imaging was performed on an N-STORM microscope (Nikon Instruments) according to ref. [66]. Briefly, MLKL WT/KO cells expressed with 3× FLAG-RIP3 with or without TNF+zVAD treatment were cultured on an eight-well chambered cover glass (Thermo Fisher). Mitochondria and FLAG-RIP3 complex were detected respectively by using primary antibodies (rabbit anti-Tomm20 (1:100, Santa Cruz) and mouse anti-Flag (1:200, CST) and fluorescent secondary antibodies (goat anti-rabbit Alexa 647(1:1,000, Thermo Fisher); goat anti-mouse Atto 488 (1:1,000, Sigma-Aldrich)). To obtain two-colour STORM images, we sequentially imaged the sample in the imaging buffer that contained 50 mM Tris (pH 8.0), 10 mM NaCl, 0.5 mg ml^{-1} glucose oxidase (Sigma-Aldrich), 40 µg ml^{-1} catalase (Sigma-Aldrich), 10% (wt/vol) glucose and 143 mM βME (Fluka). Fluorescence light was spectrally filtered with emission filters (ET525/50m and ET700/75m, Chroma) and imaged on an electron-multiplying charge-coupled device camera (iXon × 3 DU-897, Andor). Typically, 40,000–60,000 frames were collected, and images were reconstructed using the N-STORM module in NIS-Elements AR software. The same dynamic range was used for all images. Co-localization of RIP3 with mitochondria was calculated as described in ref. [67]. Briefly, high-resolution STORM images of both mitochondria and RIP3 were subjected to median filtering and intensity thresholding. Object boundaries were then determined with a size threshold of 100 nm and the whole number of RIP3 complex was calculated. Mitochondria boundaries were dilated by 1 pixel to account for erosion during boundary identification. A mitochondria–RIP3 boundary-to-boundary distance of <100 nm was defined as co-localization. The percentage of co-localization was calculated by dividing the number of mitochondria-co-localized RIP3 complexes by the whole number of RIP3 complexes.

Mitochondria depletion. The protocol was as described previously[68]. Briefly, L929 cells were infected with lentivirus encoding FLAG-Parkin and treated with CCCP (10 µM) for 48 h.

Mitochondria isolation. Mitochondria of cells were isolated as described previously[69]. Briefly, 10 plates of L929 cells (150 mm dish) were harvested with a scraper and washed twice with PBS. Cells were suspended in buffer I (225 mM mannitol, 75 mM sucrose, 0.1 mM EGTA and 30 mM Tris-HCl, pH 7.4) and homogenized with a glass homogenizer (Kontes). Samples were centrifuged at 600*g* to remove nucleus, then centrifuged at 7,000*g* to collect the crude mitochondria (pellet). For further purification, crude mitochondria were suspended in mitochondria resuspending buffer (250 mM mannitol, 5 mM HEPES, pH 7.4 and 0.5 mM EGTA) and loaded on a 20% Percoll gradient. After being centrifuged at 95,000*g* for 30 min, the pellet was collected as pure mitochondria. Equivalent amounts of protein from each fraction were analysed by SDS–PAGE and immunoblotting.

Statistics and reproducibility. Statistical analysis was performed with Prism software (GraphPad Software). Error bars represent means ± s.e.m. Each experiment was repeated three times independently with similar results. All representative experimental findings were verified in three independent experiments. Two-tailed Student's *t*-test was used to compare differences between groups. Differences in compared groups were considered statistically significantly different with *P* values lower than 0.05 (NS: no significant difference).

Life Sciences Reporting Summary. Further information on experimental design and reagents is available in the Life Sciences Reporting Summary.

Data availability. Mass spectrometry data have been deposited in ProteomeXchange under primary accession code PXD008004.

Source data for Figs. 1–7 and Supplementary Figs. 1–7 have been provided as Supplementary Table 1. Uncropped images of blots are shown in Supplementary Fig. 8. All other data supporting the findings of this study are available from the corresponding author upon reasonable request.

References

55. Chen, X. et al. Translocation of mixed lineage kinase domain-like protein to plasma membrane leads to necrotic cell death. *Cell. Res.* **24**, 105–121 (2014).
56. Zhang, D. W. et al. RIP3, an energy metabolism regulator that switches TNF-induced cell death from apoptosis to necrosis. *Science* **325**, 332–336 (2009).
57. Lin, J. et al. A role of RIP3-mediated macrophage necrosis in atherosclerosis development. *Cell. Rep.* **3**, 200–210 (2013).
58. Yoshida, S. et al. Molecular chaperone TRAP1 regulates a metabolic switch between mitochondrial respiration and aerobic glycolysis. *Proc. Natl. Acad. Sci. USA* **110**, E1604–1612 (2013).
59. Hanson, G. T. et al. Investigating mitochondrial redox potential with redox-sensitive green fluorescent protein indicators. *J. Biol. Chem.* **279**, 13044–13053 (2004).
60. Waypa, G. B. et al. Hypoxia triggers subcellular compartmental redox signaling in vascular smooth muscle cells. *Circ. Res.* **106**, 526–535 (2010).
61. Cong, L. et al. Multiplex genome engineering using CRISPR/Cas systems. *Science* **339**, 819–823 (2013).
62. Mali, P. et al. RNA-guided human genome engineering via Cas9. *Science* **339**, 823–826 (2013).
63. Zhang, F. et al. Efficient construction of sequence-specific TAL effectors for modulating mammalian transcription. *Nat. Biotechnol.* **29**, 149–153 (2011).
64. Frezza, C. et al. Haem oxygenase is synthetically lethal with the tumour suppressor fumarate hydratase. *Nature* **477**, 225–228 (2011).
65. Wu, X. et al. Investigation of receptor interacting protein (RIP3)-dependent protein phosphorylation by quantitative phosphoproteomics. *Mol. Cell. Proteom.* **11**, 1640–1651 (2012).
66. Dempsey, G. T., Vaughan, J. C., Chen, K. H., Bates, M. & Zhuang, X. Evaluation of fluorophores for optimal performance in localization-based super-resolution imaging. *Nat. Methods* **8**, 1027–1036 (2011).
67. French, J. B. et al. Spatial colocalization and functional link of purinosomes with mitochondria. *Science* **351**, 733–737 (2016).
68. Narendra, D., Tanaka, A., Suen, D. F. & Youle, R. J. Parkin is recruited selectively to impaired mitochondria and promotes their autophagy. *J. Cell. Biol.* **183**, 795–803 (2008).
69. Wieckowski, M. R., Giorgi, C., Lebiedzinska, M., Duszynski, J. & Pinton, P. Isolation of mitochondria-associated membranes and mitochondria from animal tissues and cells. *Nat. Protoc.* **4**, 1582–1590 (2009).

nature research

Corresponding author(s): Jiahuai Han

☐ Initial submission ☐ Revised version ☒ Final submission

Life Sciences Reporting Summary

Nature Research wishes to improve the reproducibility of the work that we publish. This form is intended for publication with all accepted life science papers and provides structure for consistency and transparency in reporting. Every life science submission will use this form; some list items might not apply to an individual manuscript, but all fields must be completed for clarity.

For further information on the points included in this form, see Reporting Life Sciences Research. For further information on Nature Research policies, including our data availability policy, see Authors & Referees and the Editorial Policy Checklist.

Experimental design

1. Sample size

Describe how sample size was determined.	No sample-size calculation was performed. Our sample sizes were 3 independent experiments, or 3 independent biological samples. These samples sizes are sufficient because our experiments results are stable and reproducible.

2. Data exclusions

Describe any data exclusions.	No data were excluded from the analyses.

3. Replication

Describe whether the experimental findings were reliably reproduced.	All attempts at replication of our experiments were successful.

4. Randomization

Describe how samples/organisms/participants were allocated into experimental groups.	Samples were randomly allocated to groups.

5. Blinding

Describe whether the investigators were blinded to group allocation during data collection and/or analysis.	The investigators were not blinded during data acquisition and analysis. We used cells/cell lines in our experiments. The drugs treatments and samples harvest process made it impossible to be blinded. And blinding was not relevant to our study, because we used cultured cells and all data was collected by apparatus equipment with no human bias involved.

Note: all studies involving animals and/or human research participants must disclose whether blinding and randomization were used.

6. Statistical parameters

For all figures and tables that use statistical methods, confirm that the following items are present in relevant figure legends (or in the Methods section if additional space is needed).

n/a	Confirmed	
☐	☒	The exact sample size (*n*) for each experimental group/condition, given as a discrete number and unit of measurement (animals, litters, cultures, etc.)
☐	☒	A description of how samples were collected, noting whether measurements were taken from distinct samples or whether the same sample was measured repeatedly
☐	☒	A statement indicating how many times each experiment was replicated
☐	☒	The statistical test(s) used and whether they are one- or two-sided (note: only common tests should be described solely by name; more complex techniques should be described in the Methods section)
☒	☐	A description of any assumptions or corrections, such as an adjustment for multiple comparisons
☐	☒	The test results (e.g. *P* values) given as exact values whenever possible and with confidence intervals noted
☐	☒	A clear description of statistics including central tendency (e.g. median, mean) and variation (e.g. standard deviation, interquartile range)
☐	☒	Clearly defined error bars

See the web collection on statistics for biologists for further resources and guidance.

▸ Software

Policy information about availability of computer code

7. Software

Describe the software used to analyze the data in this study.	GraphPad Prism V6; Wave 4.0; Excel 2013; BD CellQuest Pro; Image J 1.43m; NIS-Elements AR software We did not utilize any custom algorithms or software that are not yet described in the published literature.

For manuscripts utilizing custom algorithms or software that are central to the paper but not yet described in the published literature, software must be made available to editors and reviewers upon request. We strongly encourage code deposition in a community repository (e.g. GitHub). *Nature Methods* guidance for providing algorithms and software for publication provides further information on this topic.

▸ Materials and reagents

Policy information about availability of materials

8. Materials availability

Indicate whether there are restrictions on availability of unique materials or if these materials are only available for distribution by a for-profit company.	All materials are available from the authors or commercial source. No unique materials were used.

9. Antibodies

Describe the antibodies used and how they were validated for use in the system under study (i.e. assay and species).	rabbit-anti-human RIP3, abcam-ab152130 (Cambridge Cambridgeshire, UK), 1:1000 dilution;
	rabbit-anti-p-PDC-E1α(S293) (EPR12200), abcam-ab177461 (Cambridge Cambridgeshire, UK), 1:1000 dilution;
	rabbit-anti-p-PDC-E1α(S293), abcam-ab115343 (Cambridge Cambridgeshire, UK), 1:1000 dilution;
	rabbit-anti-p-PDC-E1α(S300), abcam-ab114345 (Cambridge Cambridgeshire, UK), 1:1000 dilution;
	rabbit-anti-tom20(FL145), santa cruz-sc11415 (Dallas, Texas, USA), 1:500 dilution;
	mouse-anti-GAPDH(6C5), santa cruz-sc32233 (Dallas, Texas, USA), 1:500 dilution;
	mouse-anti-FLAG, sigma-F1804 (St. Louis, MO, USA), 1:1000 dilution;
	mouse-anti-β-actin(AC-15), sigma-A1978 (St. Louis, MO, USA), 1:10000 dilution;
	mouse-anti-RIP1, BD biosciences-610456 (San Jose, CA, USA), 1:1000 dilution;
	rabbit-anti-mRIP3, raised from rabbit by using E. coli-expressed GST-RIP3 (287-387 amino acid), 1:1000 dilution;
	rabbit-anti-PDC-E1α, Proteintech-18068-1-AP (Wuhan, China), 1:1000 dilution;
	rabbit-anti-PDC-E1β, Proteintech-14744-1-AP (Wuhan, China), 1:1000 dilution;
	rabbit-anti-PDC-E2, Proteintech-13426-1-AP (Wuhan, China), 1:500 dilution;
	rabbit-anti-PDC-E3, Proteintech-16431-1-AP (Wuhan, China), 1:1000 dilution;
	rabbit-anti-LDHA, Proteintech-19987-1-AP (Wuhan, China), 1:500 dilution;

10. Eukaryotic cell lines

a. State the source of each eukaryotic cell line used.	L929, HEK293T, HeLa, HT-29 and RAW 264.7 cells were obtained from ATCC. An L929 subline that is insensitive to zVAD-induced autophagic cell death was used in our experiment. RIP1 KO, RIP3 KO, MLKL KO and 3×FLAG RIP3-reconstituted RIP3 KO L929 cells were established by CRISPR/Cas9 in our previous study. RIP3 KO RAW 264.7 cells, PDC-E1α KO, PDC-E1β KO and PDC-E3 KO L929 cells were generated by using CRISPR/Cas9 or TALEN gene editing technique. The KO cells were determined by sequencing targeted loci and western blot. RIP3 WT and KO MEFs were isolated from mouse embryos at 13.5 dpc.
b. Describe the method of cell line authentication used.	By morphology and DNA sequencing.
c. Report whether the cell lines were tested for mycoplasma contamination.	All the cell lines were repeatedly tested to be mycoplasma-free as judged by the MycoAlert™ Mycoplasma Detection Kit (Lonza, LT-07).
d. If any of the cell lines used are listed in the database of commonly misidentified cell lines maintained by ICLAC, provide a scientific rationale for their use.	No cell lines used in this study were found in the database of commonly misidentified cell lines that is maintained by ICLAC and NCBI biosample.

▸ Animals and human research participants

Policy information about studies involving animals; when reporting animal research, follow the ARRIVE guidelines

11. Description of research animals

Provide details on animals and/or animal-derived materials used in the study.	Male and female RIP3 +/- heterozygous mice (6-8 week, C57BL/6 strain) were crossed to get the embroys to generate RIP3 WT/KO MEFs and WT/KO mice to harvest peritoneal macrophages. MEFs were isolated from mouse embryos at 13.5 days post conception. Peritoneal macrophages were elicited by thioglycollate medium. We have complied with all relevant ethical regulations and all animal experimental protocols were approved by the institutional Animal Care and Use Committee at Xiamen University.

Policy information about studies involving human research participants

12. Description of human research participants

Describe the covariate-relevant population characteristics of the human research participants.	The research did not involve human research participants.

Corresponding author(s): Jiahuai Han

☐ Initial submission ☐ Revised version ☒ Final submission

Flow Cytometry Reporting Summary

Form fields will expand as needed. Please do not leave fields blank.

Data presentation

For all flow cytometry data, confirm that:

☒ 1. The axis labels state the marker and fluorochrome used (e.g. CD4-FITC).

☒ 2. The axis scales are clearly visible. Include numbers along axes only for bottom left plot of group (a 'group' is an analysis of identical markers).

☒ 3. All plots are contour plots with outliers or pseudocolor plots.

☒ 4. A numerical value for number of cells or percentage (with statistics) is provided.

Methodological details

5. Describe the sample preparation.	cells were cultured in 12-well or 6-well plates. Trypsin-digested and stained with dye before analysis.
6. Identify the instrument used for data collection.	BD FACS calibur
7. Describe the software used to collect and analyze the flow cytometry data.	BD CellQuest Pro
8. Describe the abundance of the relevant cell populations within post-sort fractions.	100%. We used authenticated cell lines in our experiments, so the purity was not a problem.
9. Describe the gating strategy used.	For ROS measurement with mitoSOX, the instrument settings were set as: Detector: FSC, Voltage: E00, AmpGain: 1.00, Mode: Lin; Detector: SSC, Volgate: 350, AmpGain: 1.00, Mode: Lin; Detector: FL2, Voltage: 550, AmpGain: 1.00, Mode: Log. We gated the living cells by selecting the cell population with FSC between 400 to 1000, and SSC between 0-700. Then these cells were detected for FL2 signal, which indicate the mitoSOX staining. For cell survival analysis by PI staining, the instrument settings were set as: Detector: FSC, Voltage: E-1, AmpGain: 5.50, Mode: Lin; Detector: SSC, Volgate: 350, AmpGain: 1.00, Mode: Lin; Detector: FL2, Voltage: 480, AmpGain: 1.00, Mode: Log; Detector: FL3, Voltage: 443, AmpGain: 1.00, Mode: Log. No gating was done. Cells with FSC between 200-800 and FL2 between 101 to 102 were defined as PI negative (living cells). The events counted with PI negative were divided by total events counted to get cell survival rate.

Tick this box to confirm that a figure exemplifying the gating strategy is provided in the Supplementary Information. ☐